Πρόγραμμα Μεταπτυχιακών Σπουδών

στη Φυσική

Τμήμα Φυσικής

Σχολή Θετικών Επιστημών

Πανεπιστήμιο Ιωαννίνων

ΜΕΤΑΠΤΥΧΙΑΚΗ ΔΙΠΛΩΜΑΤΙΚΗ ΕΡΓΑΣΙΑ (Μ.Δ.Ε)

Αριθμητική επίλυση της χρονοεξαρτημένης εξίσωσης Schrödinger για το πρόβλημα Coulomb–Stark

ΔΗΜΗΤΡΙΟΣ ΠΡΑΠΑΣ

Αριθμός μητρώου: 867

Επιβλέπων καθηγητής: Σαμουήλ Κοέν

Ιωάννινα Δεκέμβριος 2025

Postgraduate Studies

in Physics

Department of Physics

School of Sciences

University of Ioannina

MASTER THESIS

Numerical Solution of the Time-Dependent Schrödinger Equation for the Coulomb–Stark Problem

Dimitrios Prapas

ID Number: 867

Supervisor: Samuel Cohen

Ioannina December 2025

Περίληψη

Στην παρούσα εργασία μελετώνται θεωρητικά διαδικασίες μονοφωτονικής διέγερσης και φωτοϊονισμού από μία αρχική κατάσταση προς τελικές καταστάσεις Stark του ατόμου του Υδρογόνου υπό την παρουσία ομογενούς ηλεκτρικού πεδίου (πρόβλημα Coulomb-Stark). Η διέγερση επιτυγχάνεται μέσω μιας παλμικής, μονοχρωματικής φωτεινής δέσμης, δεδομένης συχνότητας και χρονικού προφίλ. Συγκεκριμένα, επιλύεται η χρονικά εξαρτημένη εξίσωση Schrödinger (TDSE), όπου, η ολική Χαμιλτονιανή, αποτελείται από τον όρο που περιγράφει το ατομικό υδρογόνο σε ομογενές ηλεκτρικό πεδίο, και τον όρο της αλληλεπίδρασής του με τη φωτεινή δέσμη. Για την αλληλεπίδραση αυτή χρησιμοποιείται η διπολική προσέγγιση. Το χωρικό τμήμα της Χαμιλτονιανής εκφράζεται σε ημιπαραβολικές συντεταγμένες, που ανταναικλούν τη συμμετρία του προβλήματος και επιτρέπουν τον χωρισμό μεταβλητών. Καταλήγουμε έτσι σε ένα σύστημα εξισώσεων μίας μόνο χωρικής συντεταγμένης, το οποίο διακριτοποιείται στον χώρο και στον χρόνο και επιλύεται αριθμητικά. Εφόσον η χωρική λύση εκτείνεται σε ένα πεπερασμένο πλέγμα, ιδιαίτερο βάρος δίνεται στην αποφυγή των ανακλάσεων που προκύπτουν συνήθως στις διαδικασίες αριθμητικής επίλυσης της TDSE . Ο κώδικας που έχει αναπτυχθεί, χρησιμοποιεί τη λύση του συστήματος και υπολογίζει την πυκνότητα ρεύματος πιθανότητας στη θέση ενός εικονικού ανιχνευτή όπου και συλλέγει σωρρευτικά το σήμα αυτό. Στην περίπτωση ενός «παλμού» laser με σταθερό χρονικό προφίλ το σήμα αναμένεται να σταθεροποιείται και το αποτέλεσμα της προσομοίωσης συγκρίνεται επιτυχώς με γνωστές λύσεις της βιβλιογραφίας, είτε για διαδιασίες ιονισμού στο συνεχές είτε ιονισμού μέσω του φαινομένου σήραγγας. Τέλος, διερευνώνται και χρονικά προφίλ που αντιστοιχούν σε τυπικότερες περιπτώσεις παλμών laser.

Abstract

In the present work, we present the theoretical investigation of single-photon excitation and photoionization processes out of an initial state to Stark final states of the Hydrogen atom in the presence of a homogeneous electric field (Coulomb-Stark problem). The excitation is achieved by means of a pulsed, monochromatic light beam, of given frequency and time profile. Specifically, the time-dependent Schrödinger equation (TDSE) is solved, where the total Hamiltonian consists of the term describing the atomic hydrogen in a homogeneous electric field, and the term of its interaction with the light beam. The latter is considered in the dipole approximation is used. The spatial part of the Hamiltonian is expressed in semi-parabolic coordinates, which reflect the symmetry of the problem and allow the separation of variables. We thus end up with a system of equations of a single spatial coordinate, which is discretized in space and time and solved numerically. Grid endpoints can act as artificial reflecting boundaries, so specialized techniques that suppress this numerical artifact had to be invoked. The code that has been developed uses the solution of the system and calculates the probability current density at the location of a virtual detector where it collects this signal cumulatively. For the case of a time profile of a laser "pulse" constant in time, where the signal is expected to attain a steady state, the solution is successfully compared with known solutions in the literature, either for ionization processes in the continuum or ionization through the tunneling effect. Finally, time profiles that correspond to more typical cases of laser pulses are also investigated.

Contents

1. Introduction

Atomic photoionization is a process of fundamental importance. In particular, studies of near-threshold atomic photoionization in the presence of a static (dc), homogeneous electric field (Stark effect), are exceptionally interesting. Hence, a lot of theoretical [1],[2] [3],[4],[5],[6],[7],[8],[9],[10],[11],[12],[13],[14] and experimental [2],[15],[16] work was and still is devoted nowadays to the spectroscopy of the Stark structure (total ionization cross sections). However, the rich phenomenology of near-threshold atomic photoionization is predominantly imprinted on the produced flux of slow (meV) electrons (differential cross sections). The projection of this flux on a two-dimensional position sensitive detector (PSD) provides photoelectron momentum distributions transversely to the dc field [17],[18],[19],[20],[21]. The latter are related to the wave functions of continuum [22],[23],[24],[25] and resonant [17],[19],[24],[25],[26],[27],[28],[29] atomic Stark states and can be manipulated via the polarization of the ionizing laser radiation [30]. Furthermore, these distributions are related to electron dynamics. While dynamical effects were probed in the past by a limited number of direct time domain measurements [31],[32],[33] such effects were more recently experimentally studied by means of spectral domain, "spectroscopic" procedures [21],[34],[35][36].

Such experimental data on electron dynamics require for their interpretation the solution of the time-dependent Schrödinger equation (TDSE), the necessary tool to construct the probability current density. Since TDSE has analytical solutions rarely and only in very simple cases, it is solved numerically with the assistance of dedicated computational methods, even for the simple hydrogen atom. There are a few theoretical time-domain studies dealing with the characteristics of the outgoing photoelectron flux on near-threshold atomic photoionization and for either hydrogen or multielectron atoms [14],[24],[27],[32],[33],[37][38],[39]. More recently, important work was published for near-threshold photodetachment in the presence of both a dc field and a slowly varying THz field [40],[41],[42]. Given the complexity of the numerical solution of TDSE even for the simple hydrogen atom and in a dc field only, the inclusion of a terahertz pulse to photoionization calculations is by no means trivial.

In fact, the present work is motivated by the desire to overcome the difficulties encountered in earlier theoretical time domain efforts where only the dc field was included [43],[44]. By successfully tackling these cases one can be more optimistic for the more challenging cases where the dc field is accompanied by a THz pulse (in our lab's plans for the near future). Therefore, the present study aims to numerically solve TDSE, simulating single-photon, near-threshold photoionization of the hydrogen atom in the presence of a dc field (Coulomb-Stark potential).

Certainly, the time-independent solution of the Coulomb-Stark problem cannot be handled perturbatively near the ionization threshold. Further, contrary to the earlier

TDSE solutions, we avoid here the use of spherical coordinates. Instead, we employ a semi-parabolic coordinate system that is better adapted to the symmetry of the problem, while being computationally advantageous. Additionally the TDSE is solved by a novel and by all accounts more accurate computational method. To further increase accuracy, special attention is given to the spatial distribution of the grid points, making use of the underlying physics.

In the following chapters we first discuss and set up (in Chapter 2) the relevant theoretical background and equations for the time-independent Coulomb-Stark problem along with the TDSE model and equations for single-photon ionization out of an initial atomic state. In Chapter 3 we provide details on the implementation and computational procedures followed for solving these TDSE equations and obtaining the outgoing electron wavepackets. In Chapter 4 we present and discuss the results of our calculations and their comparison with earlier steady state solutions. Finally, we present our conclusions and propose possible improvements and directions of further work.

2. Theory

As discussed in the Introduction, the present work is devoted to single-photon atomic ionization processes in a static electric field from an initial state ψ_i. More specifically, we are primarily interested in the hydrogenic dynamics of differential ionization cross sections. In the steady-state limit, the ionization processes are traditionally handled by the Fermi's Golden Rule [45]. This correlates ψ_i, to the wave function ψ^+_{out} of the outgoing (ionized) electron wave. One inconvenience of the Fermi's Golden Rule however, is that ψ^+_{out} is not uniquely defined [46]. Furthermore, its most frequently adopted asymptotic (large distance) form is that of a Coulomb-modified plane wave. This assumption though fails here due to the presence of the static electric field.

As a remedy to the problem, scattering theory notions are adopted and the ionization is examined here as a half-collision process. In this treatment, the key observable is the probability current density that directly depends on ψ^+_{out}, which is uniquely provided by the solution of the TDSE. Thus, the treatment of either steady state or time-dependent situations is straightforward and unified.

As mentioned above the solution of the TDSE for the hydrogenic (and non-hydrogenic) Stark problem was also reported in the past. In earlier works spherical coordinates were the standard and the TDSE was solved via the split-operator method [39]. There are three novelties that make this work unique. First, the employment of semi-parabolic coordinates, a system that better suits the symmetry of the physical problem at hand. Second, the TDSE is solved by a different and to the best of our knowledge more efficient and faster method [47]. Third, a spatial grid uniquely adapted to the peculiarities of the potential at hand, allows the coverage of large spatial distances with fewer mesh points. These three informed decisions allowed for significant improvements in the numerical algorithms with shorter execution times, relaxing computational requirements and increasing the accuracy of the solution. More details on how these choices are advantageous will be revealed in the chapters to come.

2.1. The time-independent Schrödinger equation for the Coulomb - Stark problem

The interaction of an atom with a homogeneous and static electric field $\mathbf{F}$ is known as the Stark effect. A somewhat detailed presentation of the stationary states can serve as a valuable prelude to the *hydrogenic* Stark effect's dynamics (Coulomb-Stark problem). Let's assume that the external electric field of strength F is oriented along the positive z axis ($\mathbf{F} = F\mathbf{z}$). The Schrödinger equation for this system is written as (in atomic units

-a.u.-, $\hbar = m_e = e = (4\pi\varepsilon_0)^{-1} = 1$) [1]

$$\left[-\frac{1}{2}\nabla^2 + U_{CS}(\mathbf{r}) - E\right]\psi = 0, \tag{2.1}$$

where U_{CS} the Coulomb-Stark potential,

$$U_{CS}(\mathbf{r}) = -\frac{Z}{r} + Fz, \tag{2.2}$$

E the energy, Z the nuclear charge (for Hydrogen $Z = 1$) and $r = \sqrt{x^2 + y^2 + z^2}$. From Eq. (2.2) it becomes obvious that the system does not possess the spherical symmetry of the Coulomb field due to the existence of the homogeneous external electric field. A cut of the U_{CS} potential along z-axis is depicted in Fig. 1. We may observe that the static electric field term "bends" the Coulomb potential in the negative direction of z. Two characteristic energies are noted in the figure. The zero-field ionization threshold in the absence of the electric field corresponding to $E = 0$, and the so-called saddle point energy E_{sp} that represents the field-induced lowering of the ionization limit. It is given by [2],

$$E_{sp} = -2\sqrt{ZF}. \tag{2.3}$$

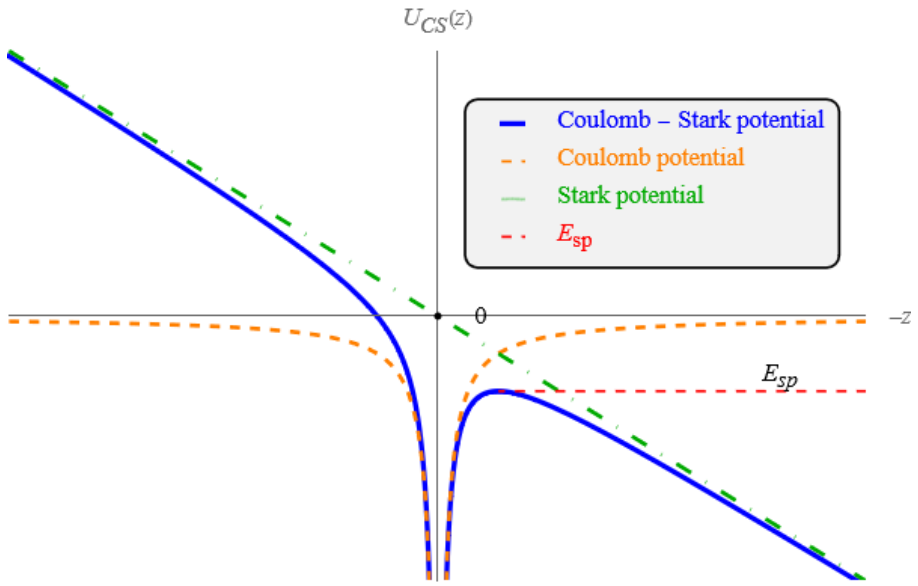

Fig. 1. *A cut of the $U_{CS}(\mathbf{r})$ potential surface along the z-axis. The saddle point energy E_{sp} is represented by the horizontal red dashed line.*

In this work we are particularly interested in the energy range $E_{sp} \leq E \leq |E_{sp}|$. Equation (2.1) is separable in semi-parabolic coordinates which reflect the symmetry of the problem [6]. They are associated with the Cartesian coordinates as follows :

$$\chi = [r + z]^{1/2} \geq 0, \quad \upsilon = [r - z]^{1/2} \geq 0 \quad \text{and} \quad \phi = \tan^{-1}\left(\frac{y}{x}\right). \tag{2.4}$$

[1] Atomic Units (a.u.) are used throughout this study, unless stated otherwise.

Eqs. (2.4) show that χ and υ have dimensions of [length]$^{1/2}$. This is quite beneficial for numerical computations over large distances. For example, $\upsilon = 200$ a.u. corresponds to a macroscopic length of ≈ 2 μm. In semi-parabolic-coordinates, the wavefunction can be written as:

$$\psi(\mathbf{r}) = (2\pi\chi\upsilon)^{-1/2} X(\chi) Y(\upsilon) e^{im\phi}, \tag{2.5}$$

where $m = 0, \pm 1, \pm 2, ...$ is the magnetic quantum number, which is a good quantum number (contrary to the orbital angular momentum quantum number ℓ, which is not [1]). Substituting equation (2.5) in (2.1), allows for the separation of variables leading to two ordinary differential equations, one for each of the wavefunctions X and Y:

$$\begin{aligned} &\left[-\frac{1}{2}\frac{d^2}{d\chi^2} + U_{X,eff}(\chi) - 2Z_1\right] X(\chi) = 0, \;\; U_{X,eff}(\chi) = \frac{4m^2-1}{8\chi^2} + \frac{F}{2}\chi^4 - E\chi^2 \\ &\left[-\frac{1}{2}\frac{d^2}{d\upsilon^2} + U_{Y,eff}(\upsilon) - 2Z_2\right] Y(\upsilon) = 0, \;\; U_{Y,eff}(\upsilon) = \frac{4m^2-1}{8\upsilon^2} - \frac{F}{2}\upsilon^4 - E\upsilon^2 \end{aligned} \tag{2.6}$$

where the separation constants Z_1 and Z_2 obey the relation:

$$Z_1 + Z_2 = Z. \tag{2.7}$$

The χ coordinate is loosely associated with a direction transverse to the electric field $\mathbf{F}$. The $X(\chi)$ wavefunction is bounded at large distances (see Fig. 2), as suggested by it's $\chi \to \infty$ asymptotic form derived from Eq. (2.6) [6],

$$X_{\chi\to\infty}(\chi) \to \frac{1}{\chi} \exp\left[-\frac{F^{1/2}}{3}\chi^3 + \frac{E}{F^{1/2}}\chi\right], \tag{2.8}$$

so $X(\chi \to \infty) \to 0$. For fixed sets of E, F and m, the desired behavior is achieved via the quantization of Z_1. Hence, Z_1 takes now a set of discrete values $Z_1^{n_1,|m|}$ and $n_1 = 0, 1, 2, ...$ corresponds to the number of nodes of $X_{n_1,|m|}$. On the other hand, at small values of χ, the term $\frac{4m^2-1}{8\chi^2}$ dominates. This term can be either a centrifugal ($|m| > 0$) or a centripetal one ($m = 0$). Again from Eq. (2.6) we find,

$$X_{\chi\to 0}(\chi) = A_X(E)\chi^{|m|+\frac{1}{2}}(1 + ...), \tag{2.9}$$

where $A_X(E)$ is an energy-dependent, and by definition positive, normalization constant, determined by the normalization condition for the wavefunction X,

$$\int_0^\infty d\chi X_{n_1,|m|}(\chi) X_{n_1',|m|}(\chi) = \delta_{n_1 n_1'}. \tag{2.10}$$

The υ coordinate is approximately associated with the direction parallel to the electric field $\mathbf{F}$. As in the χ direction, the $\frac{4m^2-1}{8\upsilon^2}$ term dominates in the vicinity of the origin and

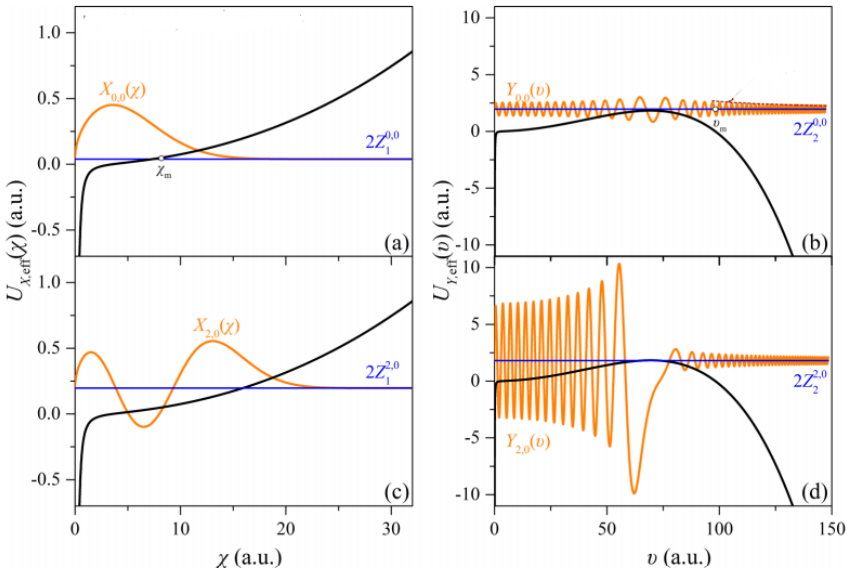

Fig. 2. *The effective potentials $U_{X,eff}(\chi)$ and $U_{Y,eff}(\upsilon)$, with the wavefunctions $X(\chi)$ and $Y(\upsilon)$ and their eigenvalues $2Z_{1,2}^{n_1,|m|}$, for $F = 808$ V/cm, $E/|E_{sp}| = -0.9565$, and $m = 0$. (a, b) The $n_1 = 0$ case, for which $2Z_2^{0,0}$ lies above the barrier of $U_{Y,eff}(\upsilon)$ and Y_{00} is a continuum wave function. (c, d) The $n_1 = 2$ case, for which $2Z_2^{2,0}$ lies slightly below the barrier. For this particular energy, Y_{20} corresponds to a quasibound state (resonance) where the electron is trapped within the inner well. For $n_1 > 2$, $2Z_2^{n_1,|m|}$ also lies below the barrier, but these states do not necessarily correspond to resonances, and the amplitude of $Y_{n_1,|m|}$ within the inner well is negligible [19].*

it can be shown that $Y(\upsilon)$ has a similar behavior with $X(\chi)$ in Eq. (2.9) that is,

$$Y_{\upsilon\to 0}(\upsilon, E) = A_Y(E)\upsilon^{|m|+\frac{1}{2}}(1 + ...), \tag{2.11}$$

where the energy-dependent normalization factor A_Y is by definition positive. As for the large distance asymptotics, the wavefunction takes the form [6],

$$Y_{\upsilon\to\infty}(\upsilon) \to \frac{1}{\upsilon}\sin\left[\frac{F^{1/2}}{3}\upsilon^3 + \frac{E}{F^{1/2}}\upsilon + \phi_0\right], \tag{2.12}$$

with ϕ_0 being a constant phase. Equation (2.12) reveals an oscillatory behavior and hence, the unbound character of Y along the υ-coordinate. A careful look to the $\frac{F^{1/2}}{3}\upsilon^3$ term in the argument of the sine function shows that at large υ the Y function oscillates at a frequency that is continuously and rapidly increasing with υ. The latter argument justifies why the numerical calculation of $Y(\upsilon)$ at large distances is considered extremely challenging requiring specialized numerical techniques [6].

The normalization factors A_X and A_Y are quite useful for characterizing a state (or channel) $||m|, n_1\rangle$ for fixed $F, |m|$ and given E, because they provide the, so-called, "Density of States" (DOS). The latter represents the probability to find the electron near the

nucleus and is given by [10],

$$\mathrm{DOS}(|m|, n_1, E) = A^2_{X,n_1,|m|} A^2_{Y,n_1,|m|}. \tag{2.13}$$

The energy dependence of DOS is better understood when we examine the $E > 0$ and $E < 0$ cases separately.

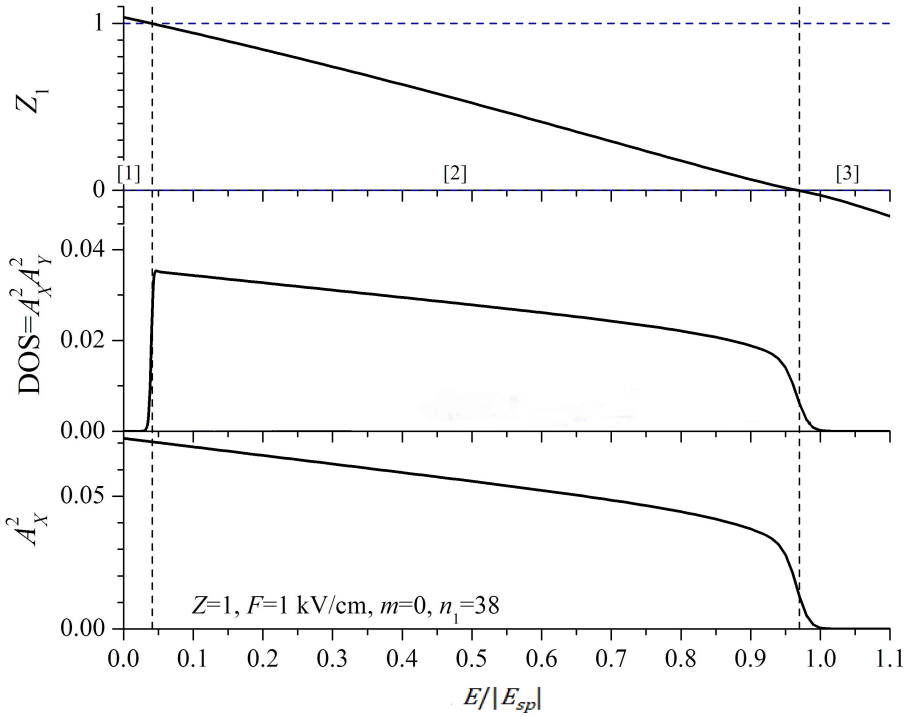

Fig. 3. *Energy variation of A^2_X, DOS and Z_1 for the $m = 0$, $n_1 = 38$ channel for $Z = 1$ and $F = 1$ kV/cm.*

Beginning with the $E > 0$ range, Fig. 3, shows the computed behavior of $Z_1(E)$, DOS and A^2_X for $Z = 1$, $m = 0$ and $n_1 = 38$. Clearly, A_X, and consequently DOS as well, become negligible when $Z_1(E) < 0$ (while A^2_Y acquires a constant non-zero value). This $Z_1 < 0$ energy range is denoted as range "[3]" in Fig. 3. In this range the specific $||m|, n_1\rangle$ state does not practically contribute to any aspect of the Physics of the Stark effect, and it is characterized as a ***closed channel***. In fact, the same happens in the range $Z_1 > Z$, but, as deduced by the behavior of A_X and DOS, it is now the A_Y factor that becomes negligible. This $Z_1 > Z$ range, denoted as range "[1]" in Fig. 3, also signals a closed channel. Hence, a channel is closed for all positive energies where either $Z_1 > Z$ or $Z_1 < 0$ holds. On the contrary, a channel is characterized as ***open*** within the energy range for which $0 \leq Z_1(E) \leq Z$ (range "[2]" in Fig. 3, that corresponds, of course, to a given range of the quantum number n_1, for fixed $|m|$). Moreover, the boundary between regions [1] and [2] ($Z_1 = Z$) is called the channel opening, while the border between regions [2] and [3] ($Z_1 = 0$) the channel closing. Note finally that all positive energy open channels are continua (***continuum channels***) since the electron escapes freely from the

atom because the potential $U_{Y,eff}(\upsilon)$ does not support bounded motion in the $E > 0$ range.

The above division to open and closed $||m|, n_1\rangle$ channels holds also for the negative energies. Now, the open channel range "[2]", is divided into two sub-regions, say [2a] and [2b] (see Fig. 4). The division point corresponds to the channel-specific threshold energy $E^{F,thr}_{n_1,|m|}$, which is the root of equation [12],[24],

$$E^{F,thr}_{n_1,|m|} = -2\left[Z_2\left(E^{F,thr}_{n_1,|m|}, F\right)F\right]^{1/2}. \tag{2.14}$$

While both $2Z_2^{n_1,|m|}$ and the top of the barrier of the potential $U_{Y,eff}(\upsilon)$ change with the energy, for $E > E^{F,thr}_{n_1,|m|}$ the channel eigenvalue $2Z_2^{n_1,|m|}$ lies always above the barrier's top. Thus, this channel is a continuum one (see Fig. 2(b)). On the other hand, for $E < E^{F,thr}_{n_1,|m|}$ (and, of course, $Z_1 < Z$, that is, within the [2a] range of Fig. 4) the eigenvalue $2Z_2^{n_1,|m|}$ lies below the barrier's top.

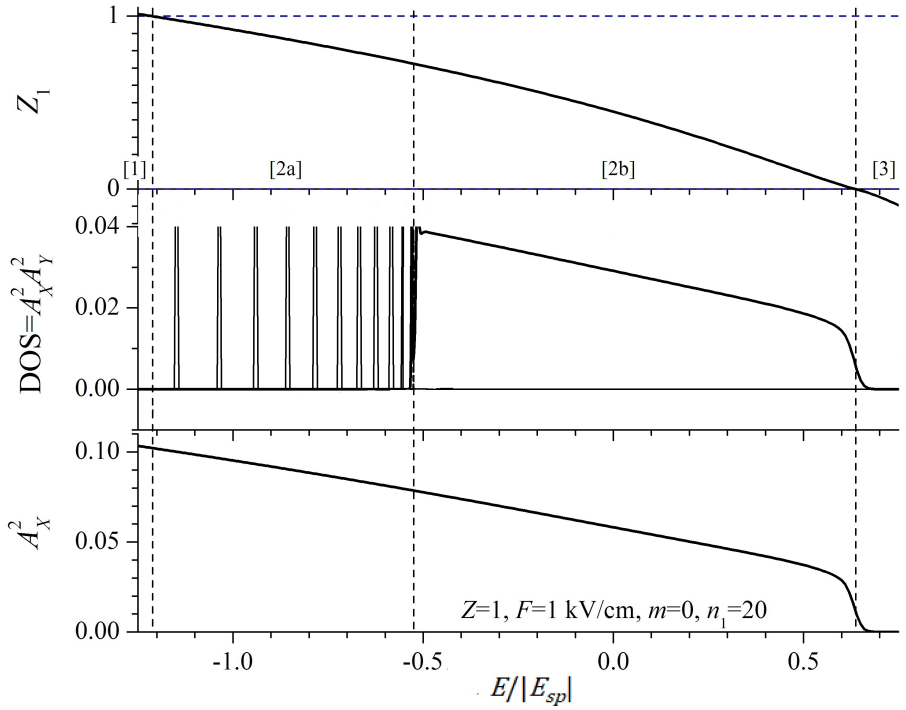

Fig. 4. *Energy variation of A_X^2, DOS and Z_1 for the $m = 0$, $n_1 = 20$, channel for $Z = 1$ and $F = 1$ kV/cm.*

In this [2a] range A_Y and consequently DOS shows a series of sharp "spectral lines" (Fig. 4). The factor A_Y acquires quite high values on the lines, while it becomes negligibly small in between them. The origin of these intense lines is the following: For $E < 0$, the potential $U_{Y,eff}(\upsilon)$ forms an inner well between the origin and the location of the top of the barrier. The well supports its own quasi-bound level eigenvalues which, however, do not necessarily coincide with the $2Z_2^{n_1,|m|} = 2\left(Z - 2Z_1^{n_1,|m|}\right)$ values *imposed* in the computation of the wavefunctions Y. Very high values of A_Y occur whenever $2Z_2^{n_1,|m|}$

coincides with one of the eigenvalues supported by $U_{Y,eff}(\upsilon)$ and the electron is trapped within the inner well (see Fig. 2(d)). When this happens, we refer to them as ***quasi-bound*** or ***resonant channels*** (or states) or simply ***resonances*** where, particularly for the *hydrogenic* Stark effect, the electron may escape from the atom solely via tunneling (Fig. 2(d)). Finally, the states in range [2a] of Fig. 4 whose energy lies in between resonances are not particularly important for the description of the Stark effect and, as said above, correspond to very small A_Y values. They are to be named hereafter simply as ***non-resonant channels***. As a first example of the above definitions, consider the energy $E = +0.5|E_{sp}|$ for $m = 0$ and $F = 1$ kV/cm, where the criterion $0 \leq Z_1 \leq Z = 1$ is fulfilled for $14 \leq n_1 \leq 53$, where all these n_1 values correspond to open, continuum channels. All other channels are closed. As a second example, consider the energy $E = -0.9564|E_{sp}|$ for $m = 0$ and $F = 808$ V/cm, where the open channels ($0 \leq Z_1 \leq Z = 1$) correspond to $0 \leq n_1 \leq 25$. Channels, $n_1 = 0$ and $n_1 = 1$ are continua, $n_1 = 2$ is a resonant channel with a relatively high value of A_Y while the rest of them are non-resonant with practically negligible A_Y factors.

2.2. Description of atomic ionization: The time-dependent Schrödinger equation and the probability current density for an effective two-level system

The study of the interaction of an atomic system with radiation and the associated dynamics requires the solution of the TDSE,

$$i\frac{\partial \Psi}{\partial t} = \hat{\mathcal{H}}\Psi, \tag{2.15}$$

where the Hamiltonian $\hat{\mathcal{H}}$ is composed by two parts, as

$$\hat{\mathcal{H}} = \hat{H}(\mathbf{r}) + \hat{V}(\mathbf{r}, t). \tag{2.16}$$

The time-independent part, $\hat{H}(\mathbf{r})$, refers to the atomic system, as well as possibly to terms related to the interaction of this system with static external fields. In the present work it is given by

$$\hat{H} = -\frac{1}{2}\nabla^2 + U_{CS}(\mathbf{r}). \tag{2.17}$$

The time-dependent part is here the interaction term between the atom and the radiation field. By adopting the dipole approximation [45], this term is written as,

$$\hat{V}(\mathbf{r}, t) = \boldsymbol{\varepsilon} \cdot \mathbf{r}\mathcal{E}_0 G(t)(e^{i\omega t} + e^{-i\omega t}), \tag{2.18}$$

where $\mathcal{E}_0$ is the field amplitude and $G(t)$ its time envelope whose amplitude is restricted within the $[0,1]$ interval.

The interaction of an atomic system with radiation may lead to coupling within a small subgroup of the atomic states, a necessary and sufficient condition for the physical process at hand. Along these lines, the presently examined single-photon ionization process may be described by an effective two-state model, comprising of an initial state ψ_i of energy E_i and a final state of an outgoing (Stark) wavepacket ψ^+_{out} of energy E. The two states are connected by the laser field, whose frequency is given by

$$\omega = E - E_i. \tag{2.19}$$

Using first order perturbation theory and the work of Ref. [39], we write the wavefunction $\Psi(\mathbf{r},t)$ of Eq. (2.15) as,

$$\Psi(\mathbf{r},t) = \psi_i(\mathbf{r})e^{-iE_it} + \psi^+_{out}(\mathbf{r},t)e^{-iEt}, \tag{2.20}$$

where it is implied that $\psi^+_{out} \propto \mathcal{E}_0$.

The initial state ψ_i can be either the ground or a low excited state of hydrogen. Such states exhibit short spatial extend and, due to the Coulomb field dominance near the origin, remain practically unaffected by the static electric field, as long as the field's strength is kept relatively low. Therefore, the electric field can be neglected in the calculation of the wavefunction of ψ_i. Nevertheless, it will be assumed here that it is, to a good approximation, an eigenstate of the Hamiltonian (2.17), that is,

$$\hat{H}\psi_i \approx E_i\psi_i. \tag{2.21}$$

Inserting Eqs.(2.16) -(2.21) to Eq. (2.15) we arrive at,

$$\left(i\frac{\partial\psi^+_{out}}{\partial t} + E\psi^+_{out}\right)e^{-i\omega t} =$$

$$\hat{H}\psi^+_{out}e^{-i\omega t} + \mathcal{E}_0\boldsymbol{\varepsilon}\cdot\mathbf{r}G(t)\left(\psi_i(e^{i\omega t}+e^{-i\omega t}) + \psi^+_{out}(1+e^{-2i\omega t})\right). \tag{2.22}$$

Keeping only the first-order terms with respect to $\mathcal{E}_0$, (and remembering that $\psi^+_{out} \propto \mathcal{E}_0$) Eq. (2.22) simplifies as follows,

$$\left(i\frac{\partial}{\partial t} + E\right)\psi^+_{out} = \hat{H}\psi^+_{out} + \boldsymbol{\varepsilon}\cdot\mathbf{r}\mathcal{E}_0G(t)(e^{2i\omega t}+1)\psi_i. \tag{2.23}$$

Furthermore, the rapidly oscillating term $e^{2i\omega t}$ can be dropped, since its contribution averages to zero. This is the rotating wave approximation (RWA) [48]. This does not

hold true for the envelope $G(t)$, which is assumed in this work to be slowly varying as compared to $1/\omega$. Let us finally define the so-called, source term,

$$S(\mathbf{r},t) \equiv \boldsymbol{\varepsilon}\cdot\mathbf{r}\mathcal{E}_0 G(t)\psi_i(\mathbf{r}), \tag{2.24}$$

where, for convenience, we set hereafter $\mathcal{E}_0 = 1$. Then, the TDSE takes the form:

$$\left(i\frac{\partial}{\partial t} - [\hat{H}(\mathbf{r}) - E]\right)\psi^+_{out}(\mathbf{r},t) = S(\mathbf{r},t), \tag{2.25}$$

which from now on, it will be called as TDSE-S (Time Dependent Schrödinger Equation with a Source) and its solution is at the core of the present work. In earlier works [19] Eq. (2.25) was solved for a radiation field characterized by an envelope constant in time, $G(t) = 1,\ \forall\, t$. In this case, the time derivative in Eq. (2.25) vanishes and a steady state is reached. The steady state version of Eq. (2.25) is written as,

$$[\hat{H}(\mathbf{r}) - E]\psi^+_{out}(\mathbf{r}) = -\boldsymbol{\varepsilon}\cdot\mathbf{r}\psi_i(\mathbf{r}) \tag{2.26}$$

and its solution is briefly presented in the Appendix.

Of interest in any photoionization calculation and/or experiment is the outgoing flux of the produced electrons. In this work we consider photoionization as a half collision process [17],[19], and this flux is obtained via the electron probability current density. The latter is defined as:

$$\mathbf{J}(\mathbf{r},t) = -\frac{1}{2i}\left[\psi^+_{out}\boldsymbol{\nabla}\left(\psi^+_{out}\right)^* - \left(\psi^+_{out}\right)^*\boldsymbol{\nabla}\left(\psi^+_{out}\right)\right], \tag{2.27}$$

and can be calculated once the TDSE-S is solved and ψ^+_{out} is known. Note that the outgoing wavepacket ψ^+_{out} in Eq. (2.27) must be necessarily complex, since otherwise the probability current is zero.

2.3. Time-discretization of the time-dependent Schrödinger equation with a source

In the absence of analytical solutions for the TDSE-S we need to discretize the time and calculate ψ^+_{out} at each time step [49]. By adopting a time grid of step Δt and deploying the, so-called, short time propagator in (2.25) [39], we obtain,

$$\psi^+_{out}(\mathbf{r},t+\Delta t) = \frac{\left(1 - i\frac{\Delta t}{2}[\hat{H} - E]\right)}{\left(1 + i\frac{\Delta t}{2}[\hat{H} - E]\right)}\psi^+_{out}(\mathbf{r},t) + \frac{i\Delta t}{2\left(1 + i\frac{\Delta t}{2}[\hat{H} - E]\right)}(S(\mathbf{r},t) + S(\mathbf{r},t+\Delta t)) \tag{2.28}$$

or

$$\left(1+i\frac{\Delta t}{2}[\hat{H}-E]\right)\psi^{+}_{out}(\mathbf{r},t+\Delta t)$$

$$=\left(1-i\frac{\Delta t}{2}[\hat{H}-E]\right)\psi^{+}_{out}(\mathbf{r},t)+i\frac{\Delta t}{2}\left(S(\mathbf{r},t)+S(\mathbf{r},t+\Delta t)\right), \tag{2.29}$$

that is the equation whose solution is required.

As a first step for solving Eq. (2.29), an appropriate matrix representation is to be chosen, for its spatial part. Then, in Eq. (2.29) the operators $\left(1+i\frac{\Delta t}{2}[\hat{H}-E]\right)$ and $\left(1-i\frac{\Delta t}{2}[\hat{H}-E]\right)$ will be square matrices and everything else will be column vectors. At each time step the solution for $\psi^{+}_{out}(\mathbf{r},t+\Delta t)$ is to be obtained, that will subsequently replace $\psi^{+}_{out}(\mathbf{r},t)$ in (2.29) and the solution will advance in time iteratively. By keeping the time-step constant, matrix $\left(1+i\frac{\Delta t}{2}[\hat{H}-E]\right)$ inversion and its multiplication by $\left(1-i\frac{\Delta t}{2}[\hat{H}-E]\right)$ are executed only once irrespectively of the number of iterations involved. To make the numerical computation easier and less time consuming we adopt the idea of Ref. [47], according to which a new wavefuction is defined as:

$$W(\mathbf{r},t+\Delta t)=\psi^{+}_{out}(\mathbf{r},t+\Delta t)+\psi^{+}_{out}(\mathbf{r},t) \tag{2.30}$$

and Eq. (2.29) takes the form,

$$\left(1+i\frac{\Delta t}{2}(\hat{H}-E)\right)W(\mathbf{r},t+\Delta t)=2\psi^{+}_{out}(\mathbf{r},t)+i\frac{\Delta t}{2}\left(S(\mathbf{r},t)+S(\mathbf{r},t+\Delta t)\right), \tag{2.31}$$

where the multiplication of the two matrices is replaced by the multiplication of a matrix with a number. Now, (2.31) is solved for $W(\mathbf{r},t+\Delta t)$ and at each time iteration $\psi^{+}_{out}(\mathbf{r},t+\Delta t)$ is recovered by means of Eq. (2.30).

2.4. Time Dependent Schrödinger Equation with a Source for the Coulomb-Stark problem in semi-parabolic coordinates

The symmetry considerations discussed in section 2.1 apply also to the Coulomb-Stark TDSE-S. Therefore, semi-parabolic coordinates are to be employed here as well, in which the initial hydrogenic wavefunction can be expressed as,

$$\psi_i(\mathbf{r})=(2\pi\chi\upsilon)^{-1/2}X_i(\chi)Y_i(\upsilon)e^{im_i\phi}, \tag{2.32}$$

either with or without the presence of the static electric field [1], and where m_i is the magnetic quantum number of ψ_i. As for the excited, outgoing, final state wavepacket, it

is written as,

$$\psi^{+}_{out}(\mathbf{r},t) = (2\pi\chi\upsilon)^{-1/2} \sum_{n'_1,m'} X_{n'_1,|m'|}(\chi) y^{+}_{n'_1,m'}(\upsilon,t) e^{im'\phi}. \tag{2.33}$$

Note that the wavefuctions X_i in Eq. (2.32) and $X_{n1',|m'|}$ in (2.33) are standard known solutions of Eq. (2.6) discussed in section 2.1. Moreover, the time-dependence in Eq. (2.33) is attached solely to the wavefunctions $y^{+}_{n'_1,m'}$ of the υ coordinate, along which ionization is allowed. Similarly, for the $W(\mathbf{r},t)$ in Eq. (2.31) we have:

$$W(\mathbf{r},t) = (2\pi\chi\upsilon)^{-1/2} \sum_{n'_1,m'} X_{n'_1,m'}(\chi) w_{n'_1,m'}(\upsilon,t) e^{im'\phi}, \tag{2.34}$$

where

$$w_{n'_1,m'}(\upsilon,t+\Delta t) = y^{+}_{n'_1,m'}(\upsilon,t+\Delta t) + y^{+}_{n'_1,m'}(\upsilon,t). \tag{2.35}$$

Inserting Eqs. (2.32)-(2.35) into TDSE-S Eq. (2.31) we arrive at,

$$\begin{aligned}
&(2\pi\chi\upsilon)^{-1/2}[\sum_{n'_1,m'} e^{im'\phi} X_{n'_1,|m'|} w_{n'_1,m'}(\upsilon,t+\Delta t) + \\
&+ \frac{i\Delta t}{2(\chi^2+\upsilon^2)} \sum_{n'_1,m'} e^{im'\phi} X_{n'_1,|m'|} \left(-\frac{1}{2}\frac{d^2}{d\upsilon^2} + U_{Y,eff}(\upsilon) - 2(Z - Z_1^{n_1,|m'|}) \right) w_{n'_1,m'}(\upsilon,t+\Delta t)] \\
&= 2(2\pi\chi\upsilon)^{-1/2} \sum_{n'_1,m'} e^{im'\phi} X_{n'_1,|m'|} y^{+}_{n'_1,m'}(\upsilon,t) + i\frac{\Delta t}{2}\left(S(\mathbf{r},t) + S(\mathbf{r},t+\Delta t)\right).
\end{aligned} \tag{2.36}$$

Now, inserting the expression for the source, acting with $\int_0^\infty d\phi \frac{e^{-im\phi}}{2\pi}$ and with $\int_0^\infty d\chi X_{n_1,|m|}$, we arrive at,

$$\begin{aligned}
&\sum_{n'_1} \left[K_{n_1,n'_1} + \upsilon^2 \delta_{n_1,n'_1} \right] w_{n'_1,m}(\upsilon,t+\Delta t) + \\
&i\frac{\Delta t}{2} \sum_{n'_1} \delta_{n'_1,n_1} \left[-\frac{1}{2}\frac{d^2}{d\upsilon^2} + \frac{4m^2-1}{8\upsilon^2} - \frac{F}{2}\upsilon^4 - E\upsilon^2 - 2(Z - Z_1^{n_1,|m|}) \right] w_{n'_1,m}(\upsilon,t+\Delta t) = \\
&2\sum_{n'_1} \left[K_{n_1,n'_1} + \upsilon^2 \delta_{n_1,n'_1} \right] y^{+}_{n'_1,m}(\upsilon,t) - i\frac{\Delta t}{2}\left(G(t) + G(t+\Delta t)\right) g^m_{n_1}(\upsilon),
\end{aligned} \tag{2.37}$$

where

$$K_{n'_1,n_1} = K_{n_1,n'_1} \equiv \int_0^\infty X_{n_1,|m|} \chi^2 X_{n'_1,|m|} d\chi \tag{2.38}$$

and

$$g^m_{n_1}(\upsilon) = Y_i(\upsilon) \int_0^\infty d\chi X_{n_1,|m|} X_i(\chi)(\chi^2+\upsilon^2) \int_0^{2\pi} d\phi \frac{e^{i(m_i-m)\phi}}{2\pi} \boldsymbol{\varepsilon}\cdot\mathbf{r}. \tag{2.39}$$

This is the system of equations to be solved with the initial condition,

$$y^{+}_{n_1',m}(\upsilon, t = t_0 = 0) = 0, \;\; \forall\, n_1', m, \tag{2.40}$$

where the initial time t_0 is set here $t_0 = 0$, so there is initially no population in any state other than the initial one. Important note, the equations that constitute the system are orthogonal with respect to the magnetic quantum number m, so for every value of $|m|$ the equations are solved separately. The function $g^m_{n_1}(\upsilon)$ originates from the spatial part of the source term, and is subjected to selection rules emerging from the ϕ-angle integral in (2.39). Note here that for odd values of m, the change $m \to -m$ leads to a simultaneous change of sign for the function $g^m_{n_1}(\upsilon)$ and the wavefunction $y^{+}_{n_1',m}(\upsilon, t)$. As for the constants $K_{n_1,n_1'}$, they couple the equations of the system (2.31). It turns out that these coupling constants are quite important for $n_1 = n_1' \pm 1$ and become practically negligible for $|n_1' - n_1| < 3$, and can be safely neglected thus leading to a sparse coupling matrix representation in the system (2.31). On the other hand, if a steady state is established, in which the wavefunction $w_{n_1',m'}(\upsilon, t)$ remains constant in time so

$$w_{n_1',m'}(\upsilon) = 2y^{+}_{n_1',m'}(\upsilon) \text{ and } G(t) = G(t + \Delta t) = 1, \tag{2.41}$$

the system of equations decouples and each equation for a given value of n_1,

$$\left[-\frac{1}{2}\frac{d^2}{d\upsilon^2} + U_{Y,eff}(\upsilon) - 2(Z - Z_1^{n_1,|m|})\right] y^{+}_{n_1,m}(\upsilon) = -g^m_{n_1}(\upsilon), \tag{2.42}$$

is solved individually (see Appendix).

Finally, since, as mentioned earlier, the electron remains bounded along the χ-direction and the ionized electron flux can emerge solely along the υ coordinate, the electron probability current density needs to be calculated on the surface of a paraboloid of constant $\upsilon = \bar{\upsilon}$ at each time t and writes,

$$J_{\bar{\upsilon}}(\phi, \chi, t) = \mathbf{J} \cdot \mathbf{e}_\upsilon = -\frac{1}{2i}\frac{1}{[\chi^2 + \upsilon^2]^{1/2}}\left[\psi^{+}_{out}\frac{\partial(\psi^{+}_{out})^*}{\partial\upsilon} - (\psi^{+}_{out})^*\frac{\partial\psi^{+}_{out}}{\partial\upsilon}\right]\Bigg|_{\upsilon=\bar{\upsilon}}, \tag{2.43}$$

with $\mathbf{e}_\upsilon$ the unit vector along the υ-coordinate. Equation (2.43) can be put in a more compact form,

$$J_{\bar{\upsilon}}(\phi, \chi, t) = -\frac{1}{[\chi^2 + \upsilon^2]^{1/2}}\mathrm{Im}\left[\psi^{+}_{out}\frac{\partial(\psi^{+}_{out})^*}{\partial\upsilon}\right]\Bigg|_{\upsilon=\bar{\upsilon}}. \tag{2.44}$$

Assuming the outgoing wavepacket ψ^{+}_{out} in (2.33) is known, we insert it to Eq. (2.44) and finally get,

$$J_{\bar{\upsilon}}(\phi, \chi, t) = -\frac{1}{2\pi\chi\upsilon[\chi^2 + \upsilon^2]^{1/2}}$$

$$\mathrm{Im}\left[\sum_{n_1',n_1,m',m} e^{i(m'-m)\phi} X_{n_1',|m'|}(\chi) X_{n_1,|m|}(\chi) y^{+}_{n_1',m'}(\upsilon,t) \frac{\partial}{\partial \upsilon}\left(y^{+}_{n_1,m}(\upsilon,t)\right)^{*}\right]\Bigg|_{\upsilon=\bar{\upsilon}}. \quad (2.45)$$

Equation (2.45) may provide the cumulative signal J_{tot} recorded over time by a virtual detector located at $\bar{\upsilon} = \upsilon_{det}$. Hence,

$$J_{tot}(\phi,\chi) = \int_0^{t_{max}} dt' J_{\upsilon_{det}}(\phi,\chi,t')), \quad (2.46)$$

where t_{max} is not necessarily infinite, but large enough for the transients to disappear and for $J_{\upsilon_{det}}$ to stop evolving with time. So it represents the total signal flux accumulated at the detector position throughout the system's temporal evolution. Finally, the total cross section can be defined as

$$\sigma_{tot} = \int_0^{t_{max}} dt' \int J_{\upsilon_{det}}(\phi,\chi,t') dS, \quad (2.47)$$

where $dS = \chi\upsilon\left[\chi^2+\upsilon^2\right]^{1/2} d\chi d\phi$ is the surface element on the υ-paraboloid. Thus, Eq. (2.47) depicts the integration of $J_{\upsilon_{det}}(\phi,\chi,t)$ over the whole surface of the detector and over the full temporal evolution of the ionization process.

3. Implementation and numerical methods

3.1. Discrete Variable Representation

The manipulations presented in the previous chapter allow the spatial dimensionality reduction from 3D to 1D (Eqs. (2.37)-(2.39)). While the υ coordinate extends over the $[0, \infty)$ interval, in practice we need to set a finite upper bound υ_{max}. Furthermore, for the spatial part of the system (2.37) (or any other similar system), a function basis must be selected that leads to a given matrix representation. Here we choose the Discrete Variable Representation (DVR) [50], due to the simplicity it offers in the representation of the operators present in our equations. As it is implied by it's name, DVR is a discretized coordinate representation over a given spatial grid, and the DVR basis functions are eigenfunctions of the coordinate operators. For a radial coordinate basis, say $|x_i\rangle$, scalar potential operators $\hat{U}$ are approximated by diagonal matrices

$$\langle x_i| \hat{U} |x_j\rangle = U(x_i)\delta_{ij}, \quad i, j = 1, 2, 3, ..., N,$$

where N is the number of grid-points, while the kinetic energy matrix $\hat{T} = \frac{1}{2}\frac{d^2}{dx^2}$ in coordinate space is approximated by a square and symmetric $N \times N$matrix:

$$T_{ij} = \langle x_i| \hat{T} |x_j\rangle = T_{ji}, \quad i, j = 1, 2, 3, ..., N. \tag{3.1}$$

By implementing an expansion over a given complete basis set, the kinetic energy matrix elements, become,

$$T_{ij} = \sum_{m,n} \langle x_i|m\rangle \langle m| \hat{T} |n\rangle \langle n|x_j\rangle . \tag{3.2}$$

In the above equation, $|m\rangle$ and $|n\rangle$ are state vectors of the chosen set, whose selection is in principle arbitrary. Here we employ a variant of DVR called Fourier Grid Method (FGM) [51], in which a Fourier basis is selected, which is associated to an even number N of plane waves in momentum space. These waves correspond to N discrete values of momentum. As a result, in the limit of infinite number of grid points $N \to \infty$, the elements T_{ij} are written as [52],

$$\begin{aligned} T_{ii} &= \frac{\pi^2}{6\Delta x^2} \\ T_{ij} &= (-1)^{i-j} \frac{1}{\Delta x^2} \frac{1}{(i-j)^2}, \; i \neq j. \end{aligned} \tag{3.3}$$

Note, however, that FGM can only be applied to equidistant grids (constant Δx). Despite their simplicity and ease of use, these grids can result in inaccurate solutions in Coulomb-like potentials [53]. This well-documented shortcoming is further discussed in

the following section along with standard methods used to alleviate the problem.

3.2. Space discretization and variable mapping

To construct an equidistant grid over the interval $[0, \upsilon_{max}]$, in order to utilize the FGM, each point should be described by

$$\upsilon_i = (i-1)\Delta\upsilon, \quad i = 1, 2, 3, ..., N, \tag{3.4}$$

with the step of size,

$$\Delta\upsilon = \frac{\upsilon_{max}}{N-1}. \tag{3.5}$$

Introducing (3.5) to (3.4) we get the form,

$$\upsilon_i = \upsilon_{max} x_i, \tag{3.6}$$

where the points x_i are given by,

$$x_i = \frac{i-1}{N-1}, \quad i = 1, 2, 3, ..., N, \tag{3.7}$$

and refer to an equidistant discretization of the dimensionless variable $x \in [0, 1]$. In fact, the discrete version of (3.6) can be associated to a continuous transformation of the form,

$$\upsilon(x) = \upsilon_{max} x. \tag{3.8}$$

Initial tests with this grid (3.6) quicly verified results from earlier studies, constant step grids can lead to inaccurate solutions [54]. The reason for this inefficiency is briefly the following: The solution of the Schrödinger (or of a Schrödinger-like) equation oscillates with a de Broglie wavelength that depends on the potential energy (here $U_{Y,eff}(\upsilon)$ of Eq. (2.6)). On the other hand, an accurate solution needs to guarantee an approximately equal number of points per wavefunction oscillation, a condition hardly achievable with constant spatial step. Many authors have shown that the problem worsens for Coulomb-like long-range potentials [53], with the present case of a static electric exacerbating the problem.

The preceding discussion underlines the need to bridge the gap between FGM's requirement for constant $\Delta x = \frac{1}{N-1}$ and the physical problem that calls for an adaptive $\Delta\upsilon$. This is possible through a, generally non-linear, variable transformation (mapping) $\upsilon \leftrightarrow x$. Thus, Eq.(3.8), which is a linear transformation needs to be generalized to,

$$\upsilon(x) = \upsilon_{max} h(x), \tag{3.9}$$

where $h(x)$ is a mapping function to be discussed in detail shortly. However, like the variable x, the function $h(x)$ is restricted to the interval $[0,1]$ with $h(0)=0$ and $h(1)=1$. It is a continuous, monotonous function, preferably differentiable up to at least third order.

Thus, the so-called mapped-FGM begins by defining the Jacobian $d\upsilon/dx$ of the transformation $\upsilon \to x$, which, using Eq. (3.9), is given by,

$$\frac{d\upsilon}{dx} = \upsilon_{max}\frac{dh}{dx} = \upsilon_{max}h'(x) = \upsilon_{max}j(x), \tag{3.10}$$

where $j(x)$ stands for a dimensionless Jacobian. Next, by following Refs. [51],[53],[55],[56] we also define the auxiliary functions Λ and λ, such that,

$$w(\upsilon,t) = [j(x)]^{1/2}\Lambda(x,t),$$

$$y^{+}_{out}(\upsilon,t) = [j(x)]^{1/2}\lambda(x,t). \tag{3.11}$$

The two functions are related by,

$$\Lambda_{n_1,m}(x,t+\Delta t) = \lambda_{n_1,m}(x,t+\Delta t) + \lambda_{n_1,m}(x,t). \tag{3.12}$$

Then, the system (2.37) is transformed to the following one,

$$\begin{aligned}
&\sum_{n_1'}\left[K_{n_1,n_1'} + \upsilon_{max}^2 h^2(x)\delta_{n_1,n_1'}\right]\upsilon_{max}^2 j^2(x)\Lambda_{n_1',m}(x,t+\Delta t) + \\
&i\frac{\Delta t}{2}\sum_{n_1'}\delta_{n_1',n_1}\left[-\frac{1}{2}\frac{d^2}{dx^2} + s(x) + \upsilon_{max}^2 j^2(x)[U_{Y,eff}(x) - 2(Z - Z_1^{n_1,|m|})]\right]\Lambda_{n_1',m}(x,t+\Delta t) = \\
&2\sum_{n_1'}\left[K_{n_1,n_1'} + \upsilon_{max}^2 h^2(x)\delta_{n_1,n_1'}\right]\upsilon_{max}^2 j^2(x)\lambda_{n_1',m}(x,t) - \\
&- i\frac{\Delta t}{2}\upsilon_{max}^2 j^{3/2}(x)\left(G(t) + G(t+\Delta t)\right)g^m_{n_1}(x),
\end{aligned} \tag{3.13}$$

where the function $s(x)$ arising in (3.13) is given by,

$$s(x) = \frac{3}{8}\left(\frac{j'(x)}{j(x)}\right)^2 - \frac{j''(x)}{4j(x)}. \tag{3.14}$$

In (3.13) we consider $\lambda(x,t)$ as a known vector, and we solve iteratively for $\Lambda(x,t)$. Similarly with (2.40), the initial condition is,

$$\lambda_{n_1',m}(\upsilon, t = t_0 = 0) = 0, \forall\ n_1', m. \tag{3.15}$$

The definitions (3.11) eliminate the first-order spatial derivative in the transformed system of Eq. (3.13). A very advantageous condition, for this particular term would have been assymetric making the numerical solution of (3.13) a lot harder to get. Finally, after

discretization using the equidistant point grid of (3.7), and recalling that (3.13) is solved at each new time step $t_{n+1} = t_0 + (n+1)\Delta t$, the system (3.13) takes the following matrix form,

$$\left[\upsilon_{max}^2 \mathbf{q}\, \mathbf{j}^2 + i\frac{\Delta t}{2}\mathbf{H} \right] \mathbf{\Lambda}^{(n+1)} =$$

$$2\upsilon_{max}^2 \mathbf{q}\, \mathbf{j}^2 \mathbf{\lambda}^{(n)} - i\frac{\Delta t}{2}\upsilon_{max}^2 [G^{(n)} + G^{(n+1)}] \mathbf{j}^{3/2} \mathbf{g}^m. \tag{3.16}$$

Both $\mathbf{q}$ and $\mathbf{H}$ are square matrices composed by the $N \times N$ square matrices $\mathbf{q}^{n_1,n_1'}$ and $\mathbf{H}^{n_1,n_1'}$, respectively, each one of the form,

$\mathbf{q} =$

	$\cdots$	$n_1' = n_1 - 1$	$n_1' = n_1$	$n_1' = n_1 + 1$	$\cdots$
$\vdots$	$\cdots$	$\cdots$	$\cdots$	$\cdots$	$\cdots$
$n_1 - 1$	$\cdots$	$\mathbf{q}^{n_1-1,n_1-1}$	$\mathbf{q}^{n_1-1,n_1}$	$\mathbf{q}^{n_1-1,n_1+1}$	$\cdots$
n_1	$\cdots$	$\mathbf{q}^{n_1,n_1-1}$	$\mathbf{q}^{n_1,n_1}$	$\mathbf{q}^{n_1,n_1+1}$	$\cdots$
$n_1 + 1$	$\cdots$	$\mathbf{q}^{n_1+1,n_1-1}$	$\mathbf{q}^{n_1+1,n_1}$	$\mathbf{q}^{n_1+1,n_1+1}$	$\cdots$
$\vdots$	$\cdots$	$\cdots$	$\cdots$	$\cdots$	$\cdots$

(3.17)

and

$\mathbf{H} =$

	$\cdots$	$n_1' = n_1 - 1$	$n_1' = n_1$	$n_1' = n_1 + 1$	$\cdots$
$\vdots$	$\cdots$	$\cdots$	$\cdots$	$\cdots$	$\cdots$
$n_1 - 1$	$\cdots$	$\mathbf{H}^{n_1-1,n_1-1}$	$\mathbf{0}$	$\mathbf{0}$	$\cdots$
n_1	$\cdots$	$\mathbf{0}$	$\mathbf{H}^{n_1,n_1}$	$\mathbf{0}$	$\cdots$
$n_1 + 1$	$\cdots$	$\mathbf{0}$	$\mathbf{0}$	$\mathbf{H}^{n_1+1,n_1+1}$	$\cdots$
$\vdots$	$\cdots$	$\cdots$	$\cdots$	$\cdots$	$\cdots$

(3.18)

with elements

$$q_{ij}^{n_1,n_1'} = \delta_{ij} \left[K_{n_1,n_1'} + \upsilon_{max}^2 h^2(x_i) \delta_{n_1,n_1'} \right], \quad i,j = 1,2,...N \tag{3.19}$$

and

$$H_{ij}^{n_1,n_1'} = \delta_{n_1,n_1'} \left[T_{ij} + \delta_{ij} \left(s(x_i) + \upsilon_{max}^2 j^2(x_i) [U_{Y,eff}(x_i) - 2(Z - Z_1^{n_1,|m|})] \right) \right], \quad i,j = 1,2,...N. \tag{3.20}$$

In Eq. (3.20) the elements of the kinetic energy matrix T_{ij} are given in (3.3). Similarly, the vector $\mathbf{\Lambda}^{(n+1)}$ is constructed by $N \times 1$ vectors $\mathbf{\Lambda}_{n_1}^{(n+1)}$ as,

$$\mathbf{\Lambda} = \left| \begin{array}{c|c} \cdots & \cdots \\ n_1 - 1 & (\mathbf{\Lambda}_{n_1-1})^{(n+1)} \\ n_1 & (\mathbf{\Lambda}_{n_1})^{(n+1)} \\ n_1 + 1 & (\mathbf{\Lambda}_{n_1+1})^{(n+1)} \\ \cdots & \cdots \end{array} \right|, \tag{3.21}$$

with elements $(\Lambda_{n_1,i})^{(n+1)}$, $i = 1, 2, ...N$. The same stands for the vectors $\boldsymbol{\lambda}^{(n)}$ and $\mathbf{g}^m$. It should be mentioned that Eq. (3.16) contains also the diagonal $N \times N$ matrices $\mathbf{j}^2$ and $\mathbf{j}^{3/2}$, multiplied by $\mathbf{q}^{n_1,n_1'}$, and by $\mathbf{g}^m$, respectively.

Finally, by defining the matrices,

$$\mathbf{A} = \left[\upsilon_{max}^2 \mathbf{q}\, \mathbf{j}^2 + i\frac{\Delta t}{2}\mathbf{H} \right] \tag{3.22}$$

and

$$\mathbf{b}^{(n)} = \left[2\upsilon_{max}^2 \mathbf{q}\, \mathbf{j}^2 \boldsymbol{\lambda}^{(n)} - i\frac{\Delta t}{2}\upsilon_{max}^2 [G^{(n)} + G^{(n+1)}] \mathbf{j}^{3/2}\, \mathbf{g}^m \right], \tag{3.23}$$

the problem is reduced to the solution of a linear system,

$$\mathbf{A}\mathbf{\Lambda}^{(n+1)} = \mathbf{b}^{(n)}, \tag{3.24}$$

with the initial conditions mentioned earlier. Matrix $\mathbf{q}$ and vector $\mathbf{g}^m$ are calculated only once for all values of n_1 and n_1' and all points of the spatial grid for all time steps. The same holds for the Hamiltonian matrix $\mathbf{H}$ (where the only difference for the different values of n_1 is the separation constant $Z_1^{n_1,|m|}$).

3.3. The mapping function

For reasons to be explained in the next chapter, the number of spatial grid points N cannot exceed 2000-2500 in our calculations. These points are to be distributed within the $[0, \upsilon_{max}]$ interval. Additionally, for field strengths of interest of the order of 1 kV/cm, $-F\upsilon^4/2$ is the dominant term of the potential $U_{Y,eff}$ already for $\upsilon \approx$ 150-250 au (1.2-3.3 μm). This spatial extent in the υ-coordinate, the potential $U_{Y,eff}$ at hand, and the modest number of grid points that can be allocated to the spatial solution calls for a judicious point redistribution through the mapping function $h(x)$.

It is frequent to base the selection of $h(x)$ on either semi-classical arguments [51],[54] or "simple" educated guesses [57]. Combining the best of the two approaches, the most

convenient ones are of the form $h(x) = x^k$, that were employed mainly [53] for potentials exhibiting an asymptotic Coulomb tail at large distances. Furthermore, these transformations were used over the full spatial range (i.e. from the origin to large distances) with a single k value. Attractive potentials demand a dense grid near the origin, so a large k is required ($k \geq 2$ or 4 etc). In this case, the grid is sparse at large distances. Repulsive potentials can be handled adequately even with $k = 1$ at short distances, but as they will become attractive at some point this option leads to degrading accuracy, making $k \geq 2$ a wiser choice.

In our case, the potential $U_{Y,eff}$ has certain particularities that make the employment of single k over the whole $[0, \upsilon_{max}]$ range prohibitive. First, depending on the value of $|m|$, it may be attractive or repulsive near the origin. Second, for negative energies a barrier is formed requiring special treatment, particularly when $2Z_2$ lies below this barrier (tunneling phenomena). Third, at large distances there is no decaying Coulomb tale, but a dominant $-F\upsilon^4/2$ term leading to a continuously decreasing de Broglie wavelength (or, classically speaking, an increasing kinetic energy) as the distance from the origin increases. Such long-range behavior calls for a progressively denser grid near υ_{max}, instead of a sparse one (that is, for example, $k < 1$).

Optimal mapping is not a well-posed problem and the search for a better one is an ongoing project. In the present work we take care of the first and the third of the above issues, knowing that our solution may not be optimal for the second issue concerning "under-the-barrier" situations.

Hence, we propose the following piecewiese mapping function,

$$h(x) = \begin{cases} p_A x^{k_A} & \text{when } 0 < x \leq x_A \\ h_{AB}(x) & \text{when } x_A \leq x \leq x_B \\ p_B(x^{k_B} - 1) + 1 & \text{when } x_B \leq x < 1 \end{cases} . \tag{3.25}$$

The form $p_A x^{k_A}$ in (3.25) ensures that $h(0) = 0$. Accordingly, the form $p_B(x^{k_B} - 1) + 1$ ensures that $h(1) = 1$. The point x_A corresponds to the location υ_A after which the centrifugal/centripetal term of $U_{Y,eff}$ has completely decayed. For $x \leq x_A$ we choose k_A=4 for m=0 and $k_A = 2$ for $|m| > 0$. Accordingly, for negative energies x_B corresponds to the point υ_B where the maximum of the barrier is located.
For the positive energies, where there is no barrier formation, x_B marks the full dominance of the $-F\upsilon^4/2$ term. In both cases, semi-classical arguments [51] suggest that, for $x \geq x_B$, $k_B = 1/3$. Once the connection between the points x_A and x_B with the points υ_A and υ_B is made the p_A and p_B parameters in Eq. (3.25) are expressed through them as follows:

$$x = x_A : \upsilon_A = \upsilon(x_A) = \upsilon_{max} h(x_A) \Rightarrow p_A = x_A^{-k_A} \frac{\upsilon_A}{\upsilon_{max}} \tag{3.26}$$

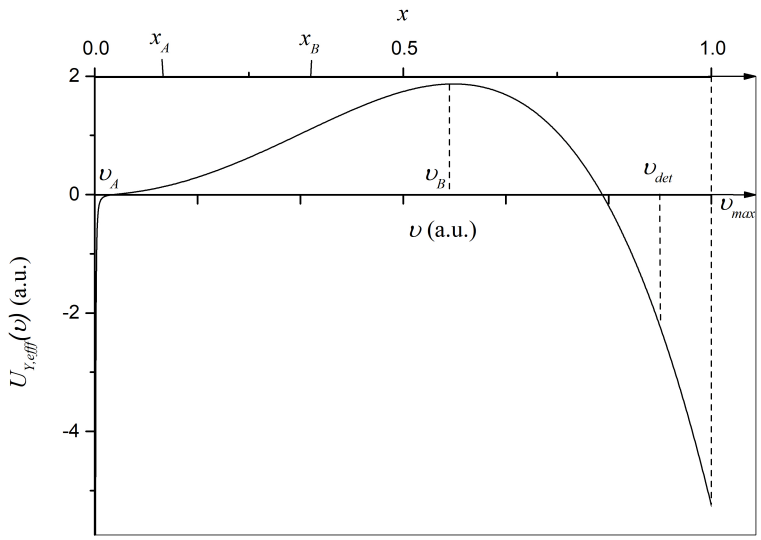

Fig. 5. *The effective potential $U_{Y,eff}(\upsilon)$, for $|m| = 0$, $F = 808$ V/cm, $E = -0.964|E_{sp}|$, $x_A = 0.11$, $x_B = 0.35$, $\upsilon_{det} = 110$ a.u.. $\upsilon_{max} = 120$ a.u., $\upsilon_A = 3.59$ a.u. and $\upsilon_B = 69.26$ a.u.*

and

$$x = x_B : \upsilon_B = \upsilon(x_B) = \upsilon_{max} h(x_B) \Rightarrow p_B = \frac{1}{x_B^{k_B} + 1} \left(\frac{\upsilon_B}{\upsilon_{max}} - 1 \right). \tag{3.27}$$

The connection function $h_{AB}(x)$ or any other relevant function in Eq. (3.25) relates x_A to υ_A and x_B to υ_B, but depends on $x_{A,B}$ parametrically. There are, in fact, several different procedures to follow for obtaining all these functions over the full interval $[0, 1]$. The most straightforward is to express $h(x)$ within the interval $[x_A, x_B]$ as a seven-degree polynomial that is differentiable up to third order and determine the polynomial's coefficients by a matching procedure to the forms of Eq. (3.25) and their derivatives at x_A and x_B. This way a relatively smooth $h(x)$ function is produced, but at the cost of a rapidly varying function $s(x)$ (Eq.(3.14)), irrespective of the choices of x_A, x_B.

Another possibility that we examined is based on the smoothness of the product $j^2(x)U_{Y,eff}(x)$ appearing in Eq. (3.13). Unfortunately, also this method resulted, under certain conditions, to functions $s(x)$ and/or $h(x)$ that were not smooth. Therefore, our presently adopted methodology uses as the first and main criterion the smoothness of the function $s(x)$. Specifically, $s(x)$ is expressed within the interval $[x_A, x_B]$ as a fifth-degree polynomial whose coefficients are determined by matching it to the forms for $x \leq x_A$ and $x \geq x_B$. For these two ranges both forms of $h(x)$ in Eq. (3.25) lead to,

$$s(x) = \frac{k^2 - 1}{8x^2}, \tag{3.28}$$

with the appropriate value of either k_A or k_B. Note that Eq. (3.28) does not contain the constants p_A, p_B. Then, a smooth trial $s_t(x_A, x_B, x)$ function is obtained that depends

parametrically on x_A, x_B. This trial function is used for solving the differential equation

$$\eta'' - 2s_t(x_A, x_B, x)\eta = 0, \tag{3.29}$$

from which we get the dimensionless jacobian function,

$$j(x) = \frac{1}{\eta^2(x)}, \tag{3.30}$$

which, along with the matching conditions,

$$j(x_A) = \frac{\upsilon_A}{\upsilon_{max}} \frac{k_A}{x_A} = \frac{1}{\eta^2(x_A)} \tag{3.31}$$

and

$$j(x_B) = k_B \frac{1 - \frac{\upsilon_B}{\upsilon_{max}}}{1 - x_B^{k_B}} x_B^{k_B - 1} = \frac{1}{\eta^2(x_B)} \tag{3.32}$$

determines $j(x)$ and from it the function $h(x)$ within the $[x_A, x_B]$ interval as,

$$h(x) = \frac{h(x_B) - h(x_A)}{\int_{x_A}^{x_B} \frac{dx'}{\eta^2(x')}} \int_{x_A}^{x} \frac{dx'}{\eta^2(x')} + h(x_A),$$

$$x_A \leq x \leq x_B,$$

$$h(x_A) = \frac{\upsilon_A}{\upsilon_{max}}, \quad h(x_B) = \frac{\upsilon_B}{\upsilon_{max}} \tag{3.33}$$

and, consequently, overall space. Nevertheless, this procedure does not guarantee the smoothness of either $j(x)$ or $h(x)$. In practice, an arbitrary value of x_A is chosen, and x_B is then varied until a smooth overall $h(x)$ function is obtained within a predefined tolerance. Unfortunately, quite frequently $j(x)$ is continuous but not smooth and the $j'(x)$ and $j''(x)$ functions are discontinuous. It should be noted that neither of the two functions is required individually, only their combination in $s(x)$ which is smooth by construction. Finally, the optimal choice of x_A, is made by minimizing the error of the electron current density, by comparing the solution of the TDSE-S with the known steady state solution discussed in the Appendix. Details and examples on the optimization procedure are given in the next chapter.

3.4. Avoiding reflections at the spatial boundary: The mask method and function

A common problem that occurs in the numerical solution of TDSE is that of the boundary conditions. Specifically, by imposing a finite $[0, \upsilon_{max}]$ spatial range, one is implicitly enclosing the computed traveling wavepacket within an infinite potential well. While this possesses no problem at $\upsilon = 0$, the "wall" at $\upsilon = \upsilon_{max}$ causes an artificial

reflection of the wavepacket. This problem is frequently rectified by either absorbing [49],[58] or transparent [47],[59] boundary conditions. Both cases are sensitive to the momentum content of the wavepacket. As a result, reflection suppression is not perfect or constant as a function of momentum. To avoid such complications, the methodology of Ref. [39] is adopted, a spatial mask function that multiplies the ongoing wavefunction after each time step. The aim of the mask is to sufficiently attenuate the wavefunction close to the $\upsilon = \upsilon_{max}$ boundary (adequately distant from the detector) in a way that at the boundary there is effectively no reflection.

Many different versions of the mask function were studied, the initial one being [39],

$$m(x) = \begin{cases} 1 & \text{if } \ 0 \leq x < x_{cut} \\ 1 - f\left(\frac{x - x_{cut}}{x_{max} - x_{cut}}\right)^2 & \text{if } \ x_{cut} \leq x \leq x_{max} \end{cases} . \tag{3.34}$$

The variable x, which appears in the mask, is the dimensionless coordinate $x \in [0, 1]$, see Eq. (3.7), f is a scale parameter that quantifies the attenuation, x_{cut} is the mask's starting point (corresponding to υ_{det}) and $x_{max} = 1$ is the last spatial grid point (υ_{max}). A similar function (4th power), was also investigated in the one-dimensional case of a free wavepacket. It was found that for $f \in [0.1, 0.6]$ the attenuation is practically independent of the initial momentum of the wavepacket. Both of these options work satisfactorily but after some experimentation we concluded that the form,

$$m(x) = \begin{cases} 1 & \text{if } \ 0 \leq x < x_{cut} \\ 1 + f\left(-12\left(\frac{x - x_{cut}}{2(x_{max} - x_{cut})}\right)^2 + 16\left(\frac{x - x_{cut}}{2(x_{max} - x_{cut})}\right)^3\right) & \text{if } \ x_{cut} \leq x \leq x_{max} \end{cases} , \tag{3.35}$$

exhibits a better performance and it is shown in Fig. 6 with the usually employed parameters $f = 0.8$, $x_{cut} = 0.8$.

Let us now discuss in more detail the parameter f. Evidently, for $f = 0$ there is no mask and reflection occurs. In fact, reflection appears even for $f = 1$, since then the mask itself functions as a "wall". As discovered by experimentation, apart from these extreme values, the masking effect is quite insensitive to f, and despite $m(x)$ being a spatial function, its reflection suppression capability is enhanced by repeatability of action. In other worlds, f is associated to the number of time steps ($= t_{max}/\Delta t$). Hence, if the number of time-steps is high enough, the number of multiplications of the wavefunction by the mask is also high, and even a mask with a small scale parameter f can, efficiently, minimize the reflection. As a rule of thump, 1000 time steps is a safe lower limit.

An example is given in Fig. 7, where we can see the $|m, n_1\rangle = |0, 0\rangle$ channel at $E = -0.967|E_{sp}|$, for two cases where t_{max} is the same. In the first case the number of steps is 5000, and in the second 200.
We can testify the absence of reflection in 7(a), when the number of time steps is large.

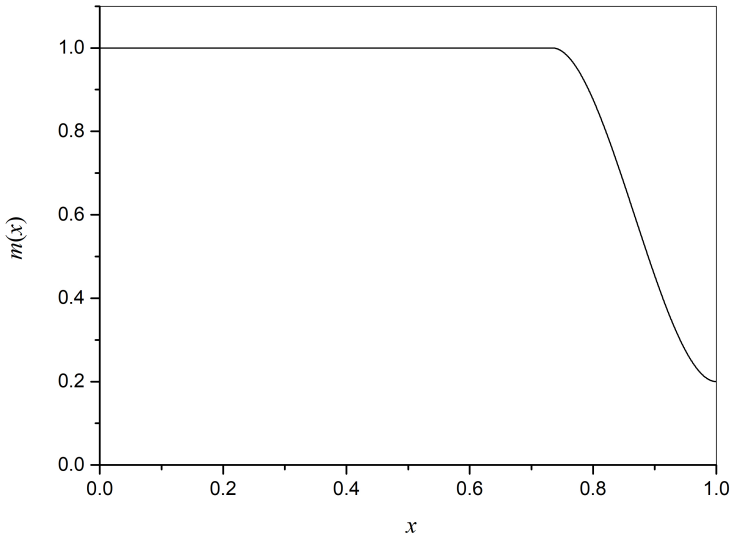

Fig. 6. *The mask function of Eq.* (3.35) *for* $f = 0.8$ *and* $x_{cut} = 0.8$.

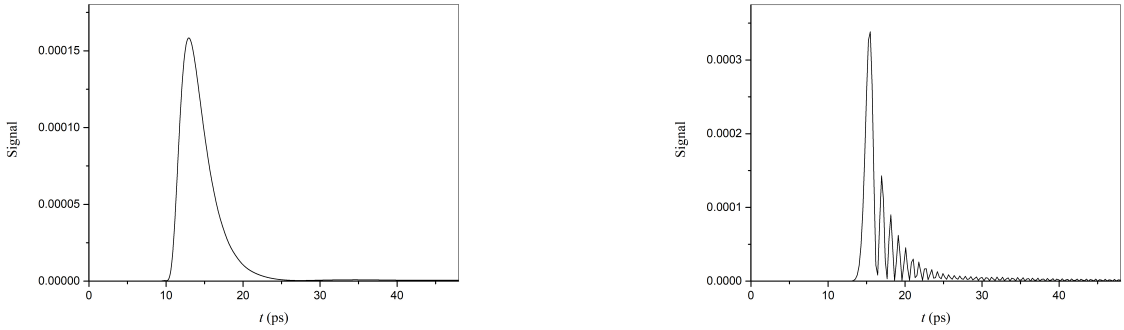

(a) ***(b)***

Fig. 7. *The time signal at* $\upsilon_{det} = 160$ *a.u. (*$\upsilon_{max} = 200$ *a.u.), for the channel* $|m = 0, n_1 = 0\rangle$ *at energy* $E = -0.967|E_{sp}|$*, with* $f = 0.8$ *and* $G(t)$ *being a bell-shaped pulse of 0.36 ps duration. In both cases* $t_{max} = 20 \cdot 10^6$ *a.u. and (a) 5000 time steps* ($\Delta t = 4000$ *a.u.) and (b) 200 time steps* ($\Delta t = 10^5$ *a.u).*

In contrast, in 7(b), the non-physical reflection by the "wall" at $\upsilon = \upsilon_{max}$ is present and manifests itself as the oscillation that appears at the right "tail" of the signal and is caused by quantum interference between the original outgoing wavepacket and the reflected one.

4. Results and discussion

4.1. Preliminary tests and remarks

Due to the $n_1 - n_1'$ coupling in Eqs. (2.37)-(2.38), the dimensions of the system (3.24) are $D \times D$, with $D = M \times N$, N the number of spatial grid points and M the number of n_1-channels included in the calculation. Our computational capabilities allow for a maximum total dimension $D = 10000$. As for M, only the open channels need to be included. In fact, by examining the A_Y values of each channel, M may, in principle, be reduced further. This assumption is, of course, to be verified later in this chapter. To understand its impact, however, consider the example given at the end of section 2.1, where for an energy $E = -0.9564|E_{sp}|$, the number of open channels is 26. Already this is a great simplification with respect to the TDSE-S solution in spherical coordinates [39],[43],[44] where M was of the order of 400 channels (corresponding to different values of orbital angular momentum quantum numbers). Nevertheless, it turns out that A_Y values are important only for $n_1 = 0 - 3$, so M can be reduced to 4. Thus, in the above example, for $D \approx 10000$ and $M = 4$ we have $N \approx 2500$. The latter is the maximum number of spatial grid points to be distributed in the interval $[0, \upsilon_{max}]$.

As already mentioned, a constant time-step greatly accelerates the temporal evolution loop, the D-matrix inversion (Eq. (3.24)) is performed only once before hand. Furthermore, after some experimentation, it was found that, if one deals solely with continuum states with quite short ionization times, $t_{max} = 20 \cdot 10^6$ a.u. and 5000 time-steps are sufficient for accurate results. On the contrary, resonances with large relaxation times require typically $t_{max} = 10^8$ a.u. and 10000 time steps. These numbers are well within the computational capabilities of a typical desktop PC, e.g. 5000 time-steps are typically performed within a few minutes.

Time envelope function $G(t)$ can take on a number of forms. The most common one writes,

$$G(t) = \frac{1}{2}\left(\mathrm{Erf}\left(\frac{\sqrt{2\ln(2)}}{t_{rise}}(t - t_{start})\right) - \mathrm{Erf}\left(\frac{\sqrt{2\ln(2)}}{t_{fall}}(t - t_{stop})\right)\right). \tag{4.1}$$

As Fig. 8 shows this function rises from 0 to 1 within t_{rise}, this rise being centered at t_{start}, where $G(t_{start}) = 0.5$. Subsequently, $G(t)$ drops from 1 to 0 within t_{fall}, while this fall is centered at t_{stop}, where again $G(t_{stop}) = 0.5$. In this work $t_{rise} = t_{fall}$. The Full Width at Half Maximum (FWHM) of this pulse is τ (FWHM)$= t_{stop} - t_{start} \geq (t_{rise} + t_{fall})/2$. If $t_{stop} - t_{start} > (t_{rise} + t_{fall})/2$ then a flat top pulse is produced, that is shaped like a trapezoid. If, on the other hand, $t_{stop} - t_{start} = (t_{rise} + t_{fall})/2$, a bell-shaped pulse is obtained that resembles a gaussian one. For bell-shaped pulses, $G(t)$ a Gaussian-type

form is used alternatively:

$$G(t) = \mathrm{Exp}\left[-4\ln(2)\left(\frac{t-t_c}{\tau}\right)^2\right]. \tag{4.2}$$

In (4.2) τ is the FWHM and t_c is the center of the pulse. Finally, if

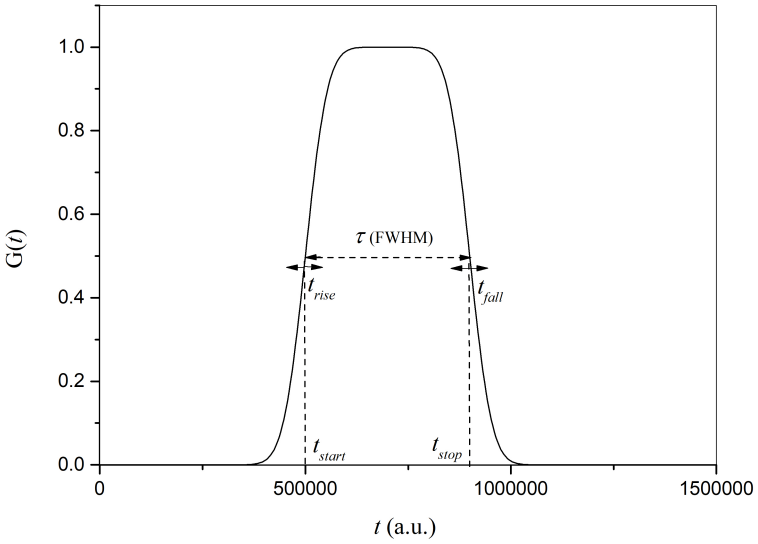

Fig. 8. *The time envelope of Eq.* (4.1) *with* $t_{start} = 5 \cdot 10^5$ *a.u.,* $t_{stop} = 9 \cdot 10^5$ *a.u. and* $t_{rise} = t_{fall} = 10^5$ *a.u.*

$t_{stop} - t_{start} >> t_{max}$ (last temporal grid point) then the pulse only rises but never falls within the calculated time interval, thus allowing a constant energy supply to the system and the simulation of steady state situations. The latter cases are are available in the literature [19], and may serve as benchmarks for our method.

Throughout this work, field strength is set to $F = 808$ V/cm and $m = 0$ identical to the values adopted in experimental and theoretical projects investigating near-threshold resonances and continuum states of the hydrogen atom [19],[27]. The same states are also studied in this work allowing for a direct comparison with the available literature. Further, it is convenient for the upcoming discussion to introduce the reduced energy variable,

$$\varepsilon = E/|E_{sp}|, \tag{4.3}$$

instead of the absolute energy E measured with respect to zero-field limit.

We select the static field axis z as the quantization axis and assume linearly polarized exciting radiation with the polarization vector $\boldsymbol{\varepsilon}$ parallel to the field direction ($\boldsymbol{\varepsilon}//\mathbf{F}$). For this a.k.a π-polarization the dipole operator writes,

$$\boldsymbol{\varepsilon} \cdot \mathbf{r} = z = \frac{\chi^2 - \upsilon^2}{2}. \tag{4.4}$$

Insertion of operator (4.4) to Eq. (2.39) leads to the selection rule $\Delta m = 0$, and, therefore, the initial and final state must have the same magnetic quantum number. Furthermore, we restrict the present study to $m = 0$ initial and final states (computationally the most challenging ones). In this case, $g^0_{n_1}$ is given by,

$$g^0_{n_1}(\upsilon) = \frac{1}{2} Y_i(\upsilon) \left[C^{(1)}_{n_1} - \upsilon^4 C^{(2)}_{n_1} \right], \tag{4.5}$$

where $C^{(1)}_{n_1}$ and $C^{(2)}_{n_1}$ are constants which are defined as,

$$\begin{aligned} C^{(1)}_{n_1} &\equiv \int_0^\infty d\chi X_{n_1,0}(\chi) X_i(\chi) \chi^4 \\ C^{(2)}_{n_1} &\equiv \int_0^\infty d\chi X_{n_1,0}(\chi) X_i(\chi). \end{aligned} \tag{4.6}$$

and are calculated numerically for each value of n_1.

We employ hydrogen field-free initial states ($m = 0$), specifically either the $n = 1$ ground state or the $n = 2$ first excited one (assuming it has been populated by some means e.g. laser excitation [27]). Specifically, in semiparabolic coordinates the ground state's X_i and Y_i components are written as [19],

$$\begin{aligned} X_i(\chi) &= 2Z\chi^{1/2} e^{-\frac{Z\chi^2}{2}}, \\ Y_i(\upsilon) &= Z\upsilon^{1/2} e^{-\frac{Z\upsilon^2}{2}}, \end{aligned} \tag{4.7}$$

while the respective components of the superposition $2^{-1/2}[|2s\rangle + |2p_{m=0}\rangle]$ [19] employed in this work (identical to the one found in experimental [27] or theoretical works [60]) are given by,

$$\begin{aligned} X_i(\chi) &= Z\chi^{1/2} e^{-\frac{Z\chi^2}{4}}, \\ Y_i(\upsilon) &= 2^{-3/2} Z\upsilon^{1/2} \left(1 - \tfrac{Z}{2}\upsilon^2\right) e^{-\frac{Z\upsilon^2}{4}}, \end{aligned} \tag{4.8}$$

As a fitting end to this section let us discuss in some detail the mapping method and its parameter selection that was briefly introduced in the previous chapter. The procedure is as follows: Beginning with a smooth function $s(x)$ (Eq. (3.14)) and once a pair of k_A and k_B is selected, a value is given to x_A. Then x_B is scanned within the interval $(x_A, 1)$ until a smooth $h(x)$ mapping function (Eq. (3.25)) is obtained within a pre-specified tolerance. When the optimum x_B is obtained for a given value of x_A, the probability current density at υ_{det} computed by solving TDSE-S under steady state conditions is compared with the corresponding Time-Independent Steady State (TISS) solution of the Appendix. Finally, the optimum value of x_A is determined by minimizing the difference between the two calculations. Figure 9 shows the variation of *Error* (defined in the graph's legend) as a function of x_A for several k_A, k_B pairs. In all cases the calculation is carried out on a 5000-point time grid, a spatial grid of 2000 points, $\upsilon_{det} = 160$ a.u. and $\upsilon_{max} = 200$ a.u.

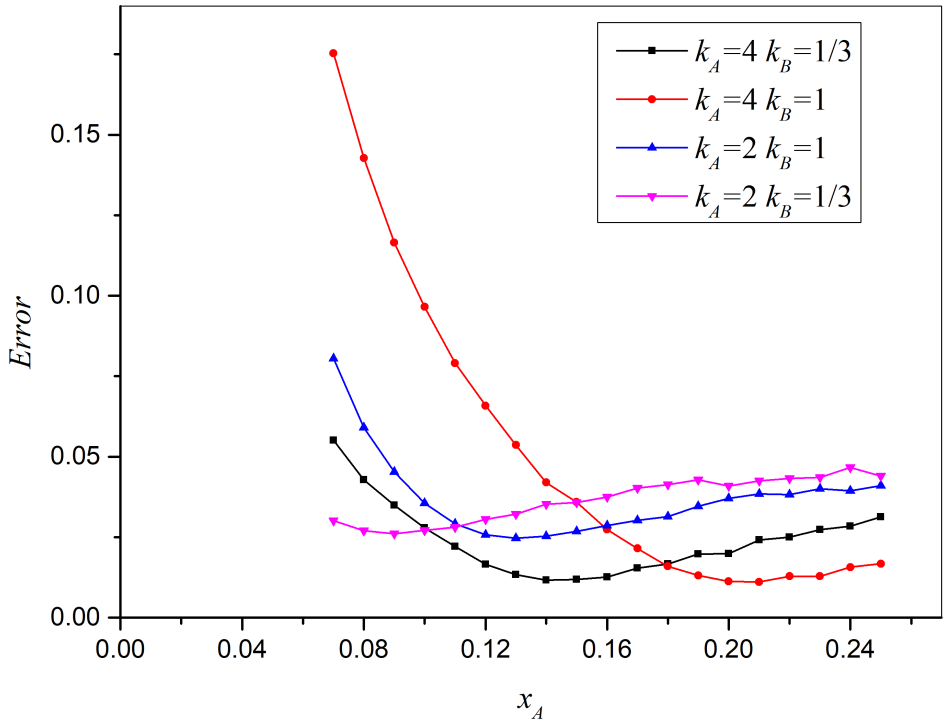

Fig. 9. *Comparison between the TDSE-S and the TISS results for the parameter x_A, with $\varepsilon = -0.9564$, $|m| = 0$, $F = 808$ V/cm for different values of k_A and k_B. The difference is calculated at each grid point as $[J_{TDSE}(x_i)^2 - J_{TISS}(x_i)^2]^{1/2}$. Those differences squared are summed, and the square root of this sum is the Error.*

Evidently $k_A = 4$ is a better choice than $k_A = 2$ (rather expected since $m = 0$). Surprisingly, the $k_A = 4, k_B = 1$ combination gives the lowest minimum *Error*. The difference from the $k_A = 4, k_B = 1/3$ pair, however, is practically insignificant, and, at present, we choose this latter pair in accordance with WKB arguments.

In connection with Fig. 5 it is noteworthy that the x-scale is connected to the v-scale in a highly nonlinear manner. For example, the optimum x_A for the $k_A = 4, k_B = 1/3$ pair acquires the quite large value of $x_A = 0.11$, which results to an almost identical signal with $x_A = 0.14$ that gives the minimum *Error* ,while the $x_B - x_A$ distance appears to contract the v_A-v_B one. More importantly, however, this optimization of the spatial grid while it is based on the steady state solution, it is expected to be valid for any excitation time profiles $G(t)$, such as the bell-shaped ones.

4.2. Steady state TDSE-S solutions

As it was mentioned earlier the TISS solutions are very important as they allow us to test the validity of our method. For the steady state solution, $G(t)$ has the functional form of Eq.(4.1) with $\tau \geq t_{max}$. This form simulates a constant energy flow to the system

and if this happens for a sufficient amount of time, (larger than the state's lifetime) temporal evolution disappears and the steady state is reached.

4.2.1. The $m = 0$ non-resonant case

A typical negative non-resonant energy, near the ionization threshold, is $\varepsilon = -0.951$ with its TISS solution documented in the literature [19]. As discussed earlier, a necessary first step before we start crunching numbers, is to identify the channels that will have an appreciable contribution to the end result. From Table 1 it can be concluded that the channels $n_1 = 0$ and $n_1 = 1$ are continua, as their respective eigenvalue $2Z_2$ is greater than the maximum of the potential. All other channels are non-resonant and only $n_1 = 2, 3$ seem to have a non-negligible A_Y value. So, only the first 4 channels ($n_1 = 0, 1, 2, 3$) seem to contribute significantly and should be taken into account for the calculation.

Furthermore, the maximum time t_{max}, that is required to reach the steady state is $20 \cdot 10^6$ atomic units of time (≈ 0.12 ns).

Table 1. *Computed nodal values for the case $Z = 1$, $m = 0$, $F = 808$ V/cm and $\varepsilon = -0.951$.*

n_1	Z_1	A_X	A_Y	$2Z_2 - U^{max}_{Y,eff}$
0	0.0194677	0.279246	1.00008	0.152289
1	0.0586083	0.280338	1.00063	0.0740075
2	0.0980513	0.281403	0.395047	−0.00487852
3	0.13779	0.282442	0.00398385	−0.0843566
4	0.177819	0.283457	0.0000803132	−0.164415
5	0.218133	0.284448	3.83664×10^{-7}	−0.245042
6	0.258725	0.285417	1.01127×10^{-8}	−0.326226
...	...	...	...	...

The temporal evolution of the total signal on the detector ($\varepsilon = -0.951$) is presented in Fig. 10.

It is evident that the system follows the behavior of the source, which continuously provides energy throughout the entire process. The beating structure is produced by the interference of the $|0, n_1\rangle$ channels. Each channel has a non-zero reflection coefficient when it reaches the potential barrier and each reflected wave oscillates with a different de Broglie wavelength, so the resulting interference, has this peculiar form. To better understand what happens lets observe each of the contributing channels separately. The continuum channels $n_1 = 0$ and $n_1 = 1$, due to their large value of A_Y are the most suitable to examine. We expect that for continuum channels, such as those two, the reflection from the barrier will be less intense, as the difference $2Z_2 - U^{max}_{Y,eff}$ becomes higher. An example is presented in Fig. 11. In this graph the eigenvalue $2Z_2$ of the channel is much higher than the barrier's top $U^{max}_{Y,eff}$, hence the reflection coefficient is almost zero, much like its classical analog. For the energy under study however, we observe a non-negligible

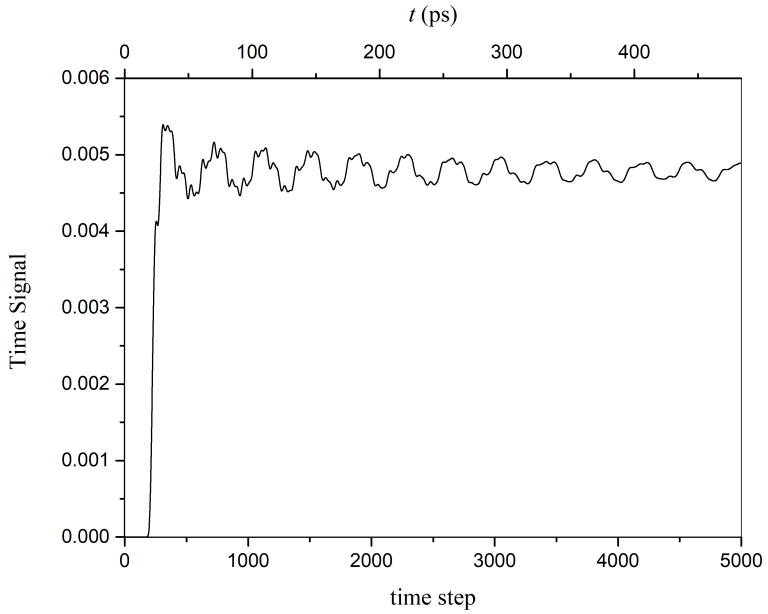

Fig. 10. *Total detector signal vs time for the non-resonant case* $\varepsilon - 0.951$*,* $F = 808$ *V/cm and* $m = 0$*, using the channels* $n_1 = 0, 1, 2, 3$*.*

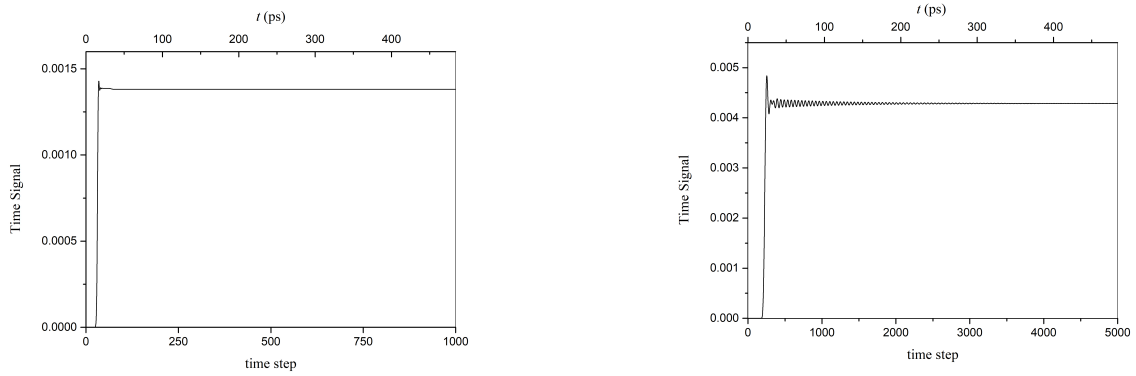

Fig. 11. *(a) Channel's* $|0, 0\rangle$ *time signal for* $\varepsilon = -0.3$*,* $F = 808$ *V/cm and* $m = 0$*, with* $2Z_2 - U^{max}_{Y,eff} = 1.79795$*. (b) Channel's* $|0, 0\rangle$ *time signal for* $\varepsilon = -0.951$*, with* $2Z_2 - U^{max}_{Y,eff} = 0.152289$*.*

percentage of reflection, since the eigenvalues of the continuum channels are much closer to the maximum value of the potential. The total detector signal versus time for the same energy can be seen in 12(a) and in 12(b), respectively, for $n_1 = 0$ and $n_1 = 1$. The signal of $n_1 = 1$ has a more intense oscillatory behavior, as was expected, because the eigenvalue $2Z_2^{1,0}$ has a value that is closer to the potential's maximum, than $2Z_2^{0,0}$. The interference of these channels appears in 12(c). If we also include $n_1 = 2$ channel then, we get the result of Fig. 10. Incorporating channel $n_1 = 3$ has no noticeable effect to the total signal, since its A_Y value is significantly smaller than the others.

Finally, the total cumulative signal for different coupled channels, appears in Fig. 13

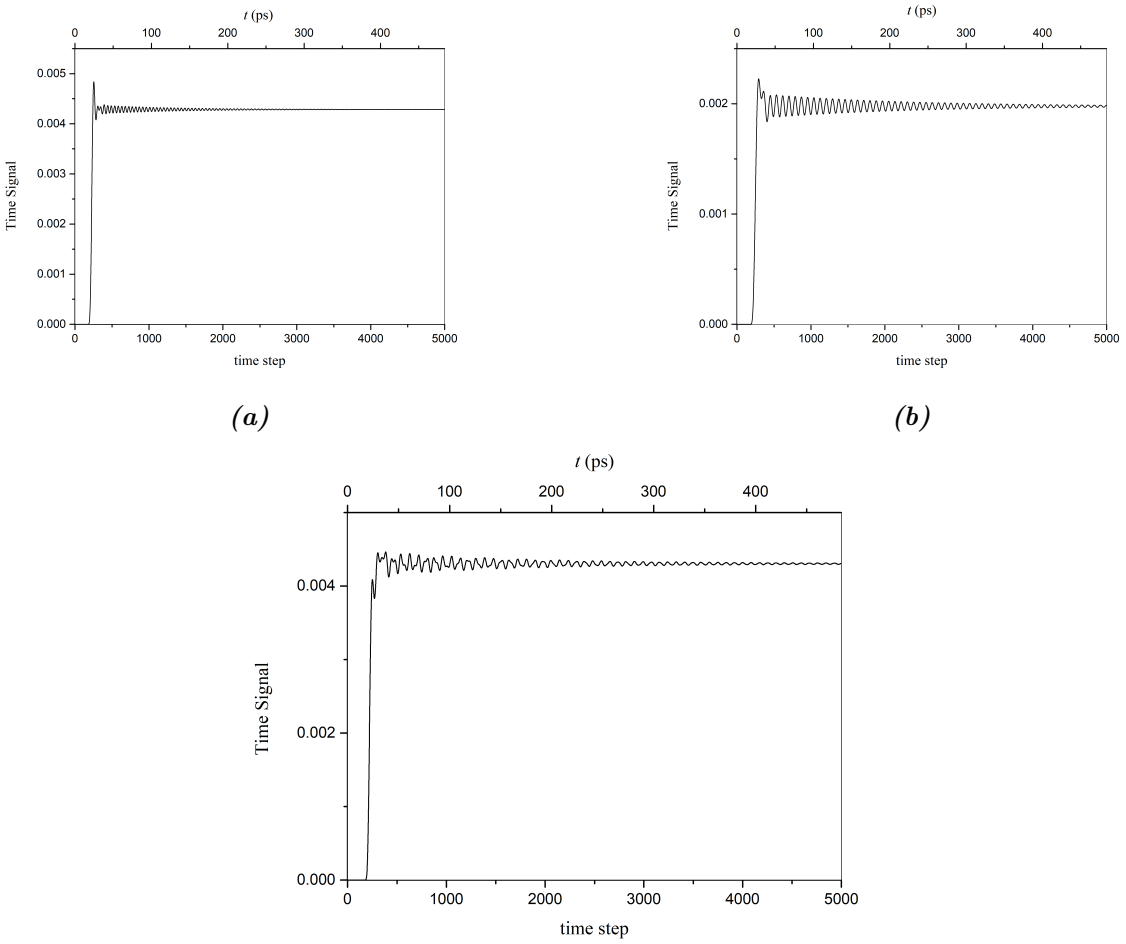

Fig. 12. *Total detector signals vs time for the non-resonant case ($\varepsilon = -0.951, F = 808\,V/cm$, $m = 0$) and for the channels (a) $n_1 = 0$, (b) $n_1 = 1$ and (c) $n_1 = 0, 1$.*

alongside the TISS results. It is worth mentioning that the TISS results include all the 26 open channels, which are produced by the program.

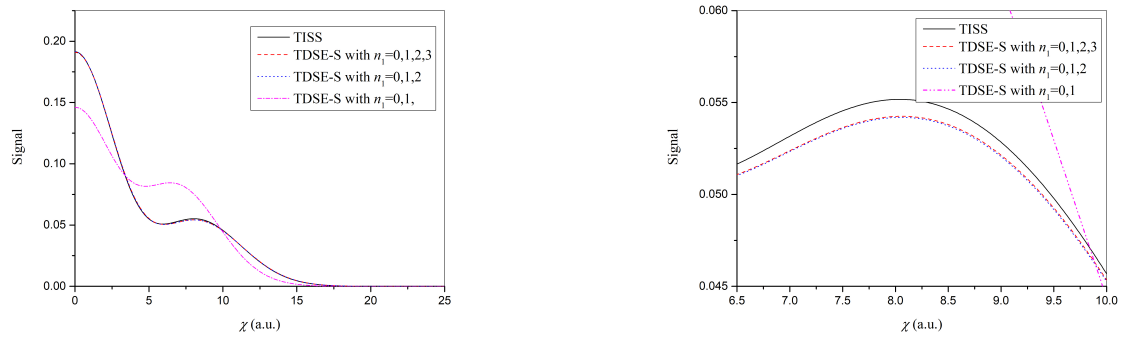

Fig. 13. *(a) The cumulative signal at the detector ($\varepsilon = -0.951$, $F = 808$ V/cm and $m = 0$) for different coupled channels alongside the TISS result (b) Magnification of (a)*

We can now conclude that incorporating only 4 channels in the calculation is a valid

approximation, since, they can accurately reproduce the TISS results. In the magnified view of Fig. Fig. 13(b) there is graphical evidence of the insignificant changes to the signal between 3 and 4 coupled channels. This, however, was expected as the factor A_Y for the $|0,3\rangle$ channel is three orders of magnitude smaller than that of the $|0,0\rangle$ and $|0,1\rangle$ channels.

4.2.2. The $m = 0$ resonant case

By far, the most interesting and intriguing cases are the resonances. With the parameters of section 4.1, a resonance exists at $\varepsilon = -0.9564$. As a preview of what follows, these unique cases require special treatment, as their numerical solutions with the proposed method do not present the kind of accuracy the non-resonant cases enjoyed.

The first step, as before, is to decide which channels should be included in the TDSE-S solution. Based on Table 2, the first two channels ($n_1 = 0, 1$) are continua and must be included in the calculation. Channels $n_1 \geq 3$ are non-resonant with very small values of A_Y and we keep only $n_1 = 3$. The most important channel, however, is $n_1 = 2$. It's a resonant channel, testified by the sharp increase in the value of A_Y and its long lifetime as it will be shown shortly. Once again, we use four channels with $n_1 = 0, 1, 2, 3$. We

Table 2. *Computed nodal values for the case $\varepsilon = -0.9564$.*

n_1	Z_1	A_X	A_Y	$2Z_2 - U^{\max}_{Y,eff}$
0	0.0195225	0.279637	0.999663	0.131579
1	0.0587714	0.280721	1.04948	0.0530811
2	0.0983212	0.281779	6.25222	−0.0260184
3	0.138165	0.282812	0.00166875	−0.105707
4	0.178298	0.283820	0.0000131222	−0.185973
5	0.218714	0.284805	1.6814×10^{-7}	−0.266804
6	0.259407	0.285769	1.26734×10^{-9}	−0.348191
...	...	...	...	...

still aim at reaching the steady state, so we will use the time envelope $G(t)$ of Eq. (4.1), again with $\tau \geq t_{max}$ but this time $t_{max} = 10^8$ a.u. or ≈ 2.42 ns. The maximum time of the calculation, has been significantly increased in comparison with the non-resonant case. This is dictated by the large lifetime that characterizes a resonant energy. The time signal of the virtual detector can be seen in Fig. 14.

The initial surge on the recorded signal subsides with time and eventually reaches its steady state value. This signal is again a result of interference between the four channels, though closer inspection of the individual contributions (Fig. 15) helps identify $n_1 = 2$ as the main contributor.

Continuum channels, $n_1 = 0, 1$ (Figs. 15(a) and 15(b)), exhibit the same signal structure as in the non-resonant case. Channel $n_1 = 3$ (Fig. 15(d)) has an almost negligible contribution to the total detector signal, as was expected by its A_Y. As for

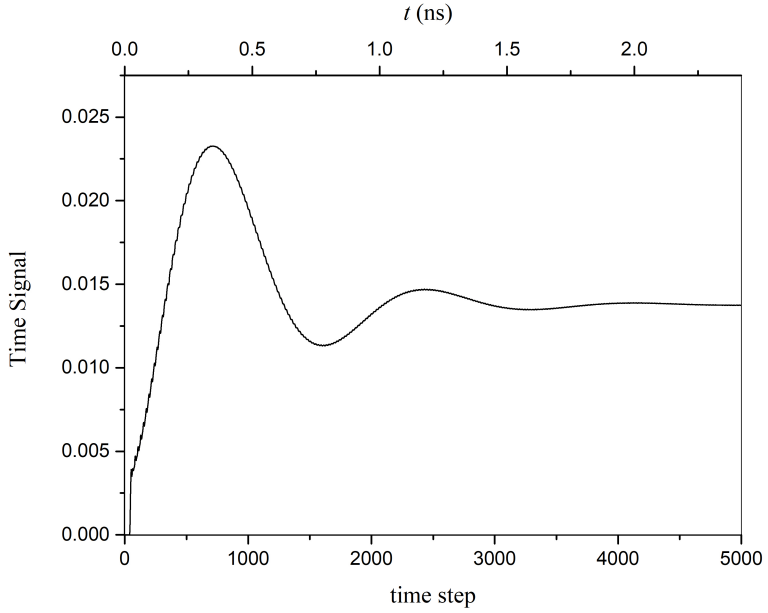

Fig. 14. *The signal over time at the detector for* $\varepsilon = -0.9564, F = 808$ *V/cm and* $m = 0$ *using the channels* $n_1 = 0, 1, 2, 3$.

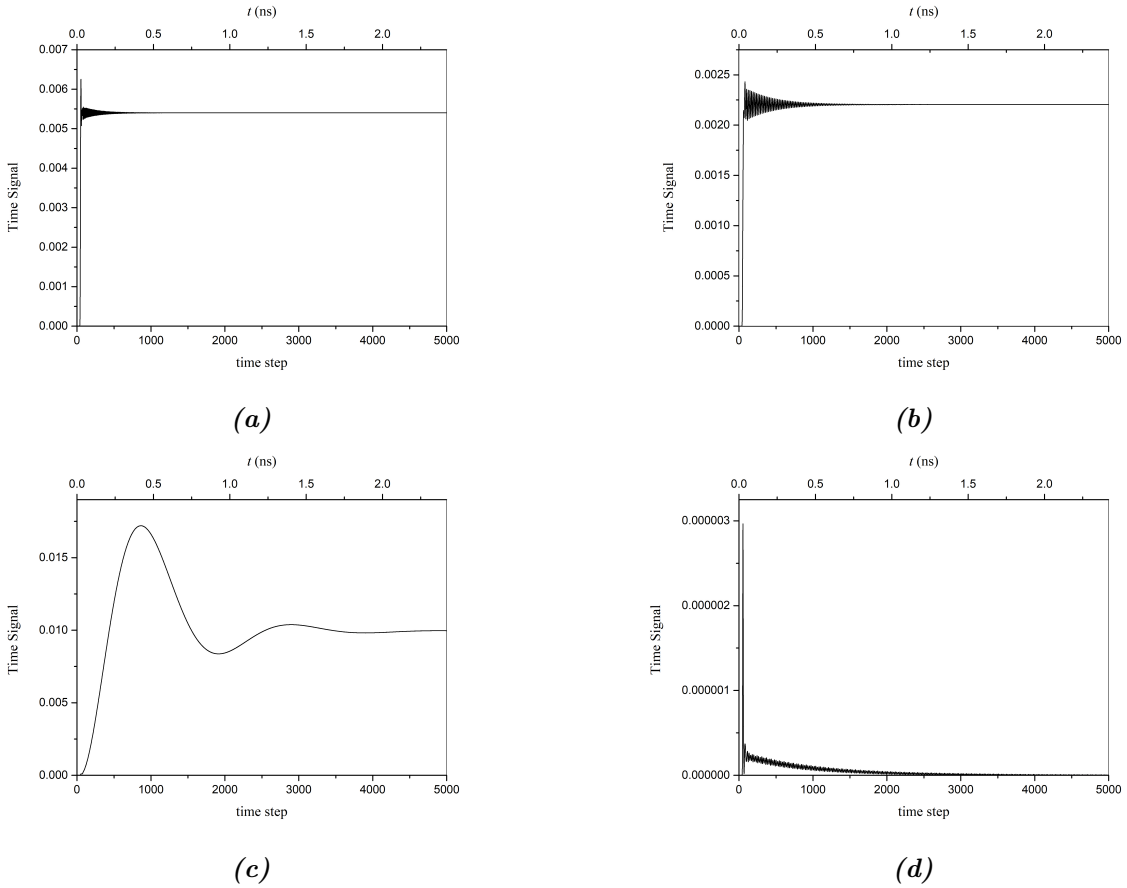

Fig. 15. *Detector's signal vs time for the energy* $\varepsilon = -0.9564$, $F = 808$ *V/cm,* $m = 0$ *and for the channel (a)* $n_1 = 0$, *(b)* $n_1 = 1$, *(c)* $n_1 = 2$ *and (d)* $n_1 = 3$.

the channel $n_1 = 2$, its signal alone is $3\times$ more intense than the signal of the second in contribution channel, $n_1 = 0$. In addition, the form of Fig. 15(c) is almost identical with Fig. 14, a fact that again attests the resonance domination.

Now, the cumulative (temporal integration) signal on the detector vs the $x \propto \rho$-coordinate is presented in figure 16, again alongside the TISS solution.

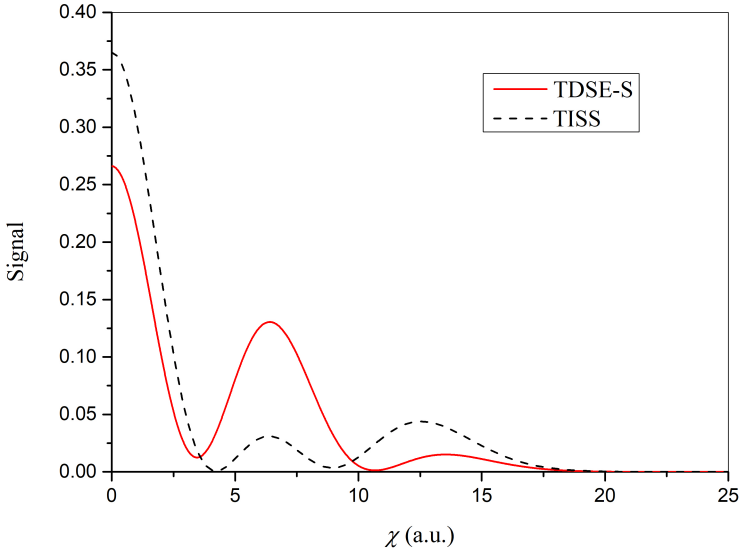

Fig. 16. *Comparison of the TDSE-S (calculated using the channels $n_1 = 0, 1, 2, 3$) and the TISS results for $\varepsilon = -0.9564$, $F = 808$ V/cm and $m = 0$.*

In this case the results exhibit significant differences, that can be attributed to the complex nature of the resonance. Nevertheless, the quality characteristics are present. There are 3 local maxima at approximately the expected places. One could expect that by increasing the numerical precision (i.e more spatial points) the time dependent curve will approach the TISS one. As stated earlier, improving the spatial mesh is constrained by the available computational resources. A quick calculation can be enlightening. In Fig. 16 we used 2000 grid points with 4 active channels (n_1) leading to a square D matrix of size 8000 by 8000 filled with complex numbers for an approximate size of 1GB. If we increase the spatial precision 5-fold that would swell the D-matrix size to a whopping size of 25 GB. As a result the computational power to handle such matrices is enormous. To further illustrate the significance of the number of grid points we can easily go the other way, lowering to 500 points per channel as it is portrayed in Fig. 17.

Now, even the quality agreement degrades. Of course, let's not forget that spatial accuracy depends also on the mapping function, the transformation of coordinates that intelligently redistributes the same number of grid points to locations where they are most effective in catching the variations of the potential energy. As was mentioned in chapter 3, when the eigenvalue $2Z_2$, lies below the barrier, which is formed for $\varepsilon < 0$, the solution requires special treatment, that is a subject of an ongoing investigation. Despite

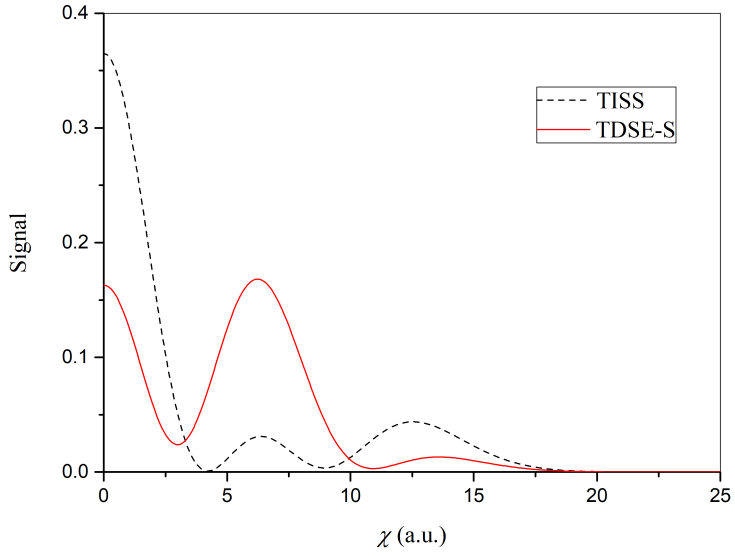

Fig. 17. *Comparison of the TDSE-S (calculated using the channels $n_1 = 0, 1, 2, 3$) and the TISS results for $\varepsilon = -0.9564$, $F = 808$ V/cm, $m = 0$ and 500 spatial grid points per channel.*

all, our mapping, manages to capture to a certain degree the de Broglie's wavelength variations. Specifically, it captures correctly the nodal behavior of the wavepacket at the resonance and can correctly reproduce the TISS results at energies just above (or below) of it. To drive the point home, a fairly naive mapping function like $h(x) = x^2$ (used in the initial tests) leads to a complete washing out of all the quality characteristics, having no resemblance to the TISS curve.

4.3. TDSE-S solutions for a laser pulse

With the method that was developed throughout the previous chapters, we are able to solve the TDSE-S, for a variety of time envelopes $G(t)$, provided that it is slowly varying in comparison with $1/\omega$. A $G(t)$ that was extensively used in tests is that of a short pulse with flattened top (a.k.a. trapezoid pulse), as in Fig. 8. This pulse can be described by equation 4.1. By setting $t_{stop} = t_{max} + 4 \cdot 10^5$ a.u., a pulse of 10 ps is created. Another example of a pulse is the Gaussian pulse (Fig. 18) with the functional form of Eq. (4.2), the duration of which, can be controlled directly from τ.

Pulse shaped sources were simulated with the same parameters and energies that were used in the steady state tests. If by increasing the pulse duration we can match the steady state results, the method is validated and can be confidently used in analyzing the temporal dynamics of the driven system.

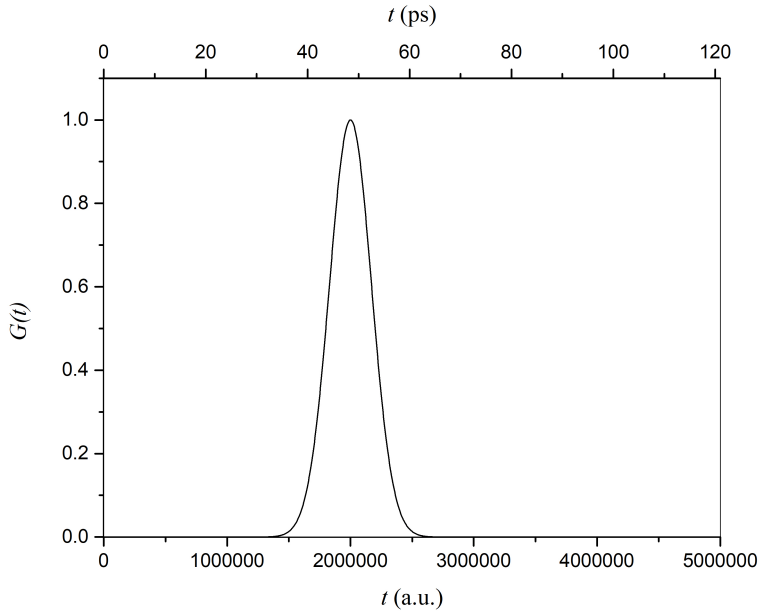

Fig. 18. *A Gaussian pulse of τ =10 ps (400000 a.u) centered at $t_c = 2 \cdot 10^6$ a.u..*

4.3.1. The $m = 0$ non-resonant case

We begin, as before, with the non-resonant energy $\varepsilon = -0.951$ and for the trapezoid pulse. Although the pulse is short-lived we let the TDSE-S follow the system for a long time, $t_{max} = 20 \cdot 10^6$ a.u. Again, only channels with significant contributions will be kept, (n_1=0,1,2,3).

The detector's signal, at $\upsilon_{det} = 160$ a.u, is depicted in Fig. 19. One can easily assign the double peak structure of the signal to the two continuum channels ($n_1 = 0, 1$) while the third local maximum is attributed to the $n_1 = 2$ non-resonant channel. A small but discernible contribution from the $n_1 = 3$ channel can also be identified, its faint signature justified by the corresponding small value of A_Y (see Table 1).

The use of pulsed sources (as in the signal of Fig. 19) serves as an excellent tool for the effectiveness of the adopted masking. The absence of a reflected wave ensures once again that the mask works as designed.

In Fig. 20 we present in a common plot the cumulative signal on the detector both for a pulsed and a steady state source. Though the two signals differ, this is to be expected. By increasing the pulse duration, we can see the pulsed source signal approach the steady state one.

Specifically, it seems that the steady state is reached even with a pulse of 0.5 ns. So $t_{max} = 0.5$ ns, is also a sufficient amount of time for the solution. The same results can be produced if we use the Gaussian pulse of equation (4.2).

Again, the steady state is reached with a Gaussian pulse of $\tau \approx 0.5$ ns. Both pulsed-source tests provide a further verification of the validity of our methodology. To conclude, the developed TDSE-S solution, is highly efficient in the energy range $\varepsilon < -0.9$ and for

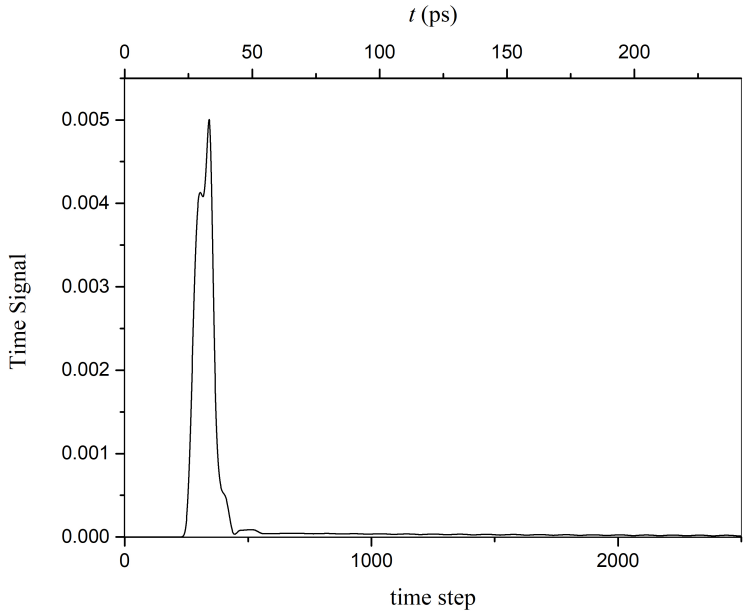

Fig. 19. *The time signal at the detector ($\varepsilon = -0.951$, $F = 808$ V/cm, $m = 0$ and four coupled channels $n_1 = 0, 1, 2, 3$) for the case of the pulse of Eq.* (4.1)*, with $\tau \approx 10$ ps.*

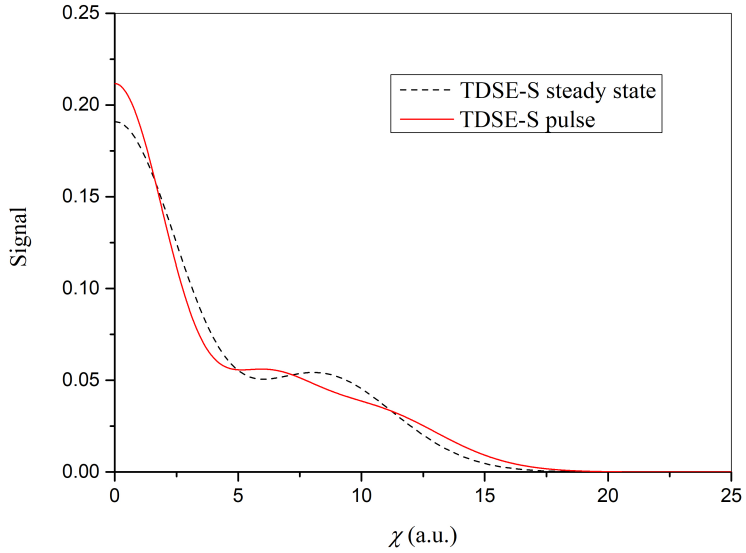

Fig. 20. *The cumulative signal at the detector for $\varepsilon = -0.951, F = 808$ V/cm and $m = 0$ in the case of a 10 ps-pulse (Eq.* (4.1)*), calculated using the channels $n_1 = 0, 1, 2, 3$, alongside the steady state results.*

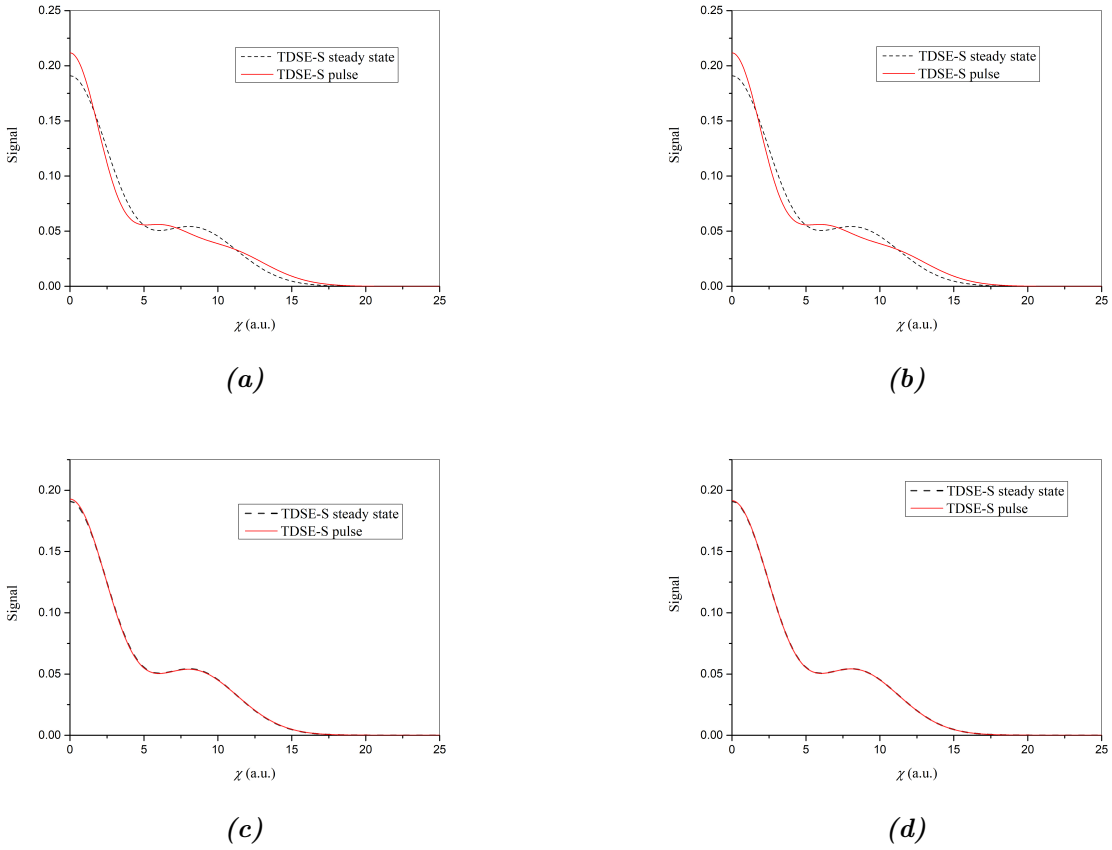

Fig. 21. *The cumulative signal (coupled channels $n_1 = 0, 1, 2, 3$) for $\varepsilon = -0.951$, $F = 808$ V/cm and $m = 0$ and for different pulse duration (Eq. (4.1)), $\tau \approx$ (a) 10 ps (b) 0.125 ns (c) 0.25 ns (d) 0.5 ns, compared with the steady state results.*

$m = 0$, as the agreement with the TISS results attested, both with a constant energy supply and with a pulse of gradually increased duration.

4.3.2. The $m = 0$ resonant case

The same time envelopes are used for the solution of the TDSE-S and for the resonant energy, $\varepsilon = -0.9564$. The pulses now last approximately 25 ps (or 10^6 atomic units of time) and the system is recorded up to $t_{max} = 10^8$ a.u, due to the greater lifetime, as was mentioned before. Again we incorporate the four channels identified also in the steady state case (Table 2) that have the largest A_Y values, with the resonant $n_1 = 2$ one having the largest value of all. Every other parameter is fixed as usual.

We start the investigation again from the pulse of Eq. 4.1, with $t_{start} = t_{stop} + 10^6$ a.u. As duly noted before, resonant channels suffer from lower accuracy, that's why this time we don't compare to the TISS signal but to the steady state TDSE-S. Over time, the detector accumulates the signal of Fig. 23(a).

The observable maxima in the time signal plot, reflect the existence of the three most dominant channels (n_1 =0,1,2) that were taken into account in the TDSE solution. The time signal is additionally presented in a logarithmic scale, in Fig. 23. The gradual

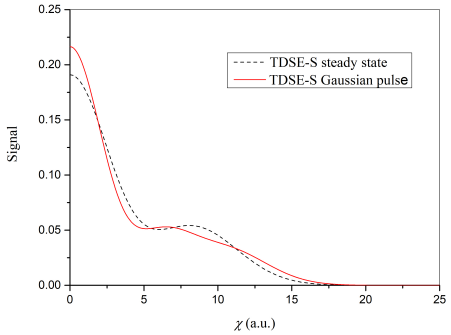

(a)

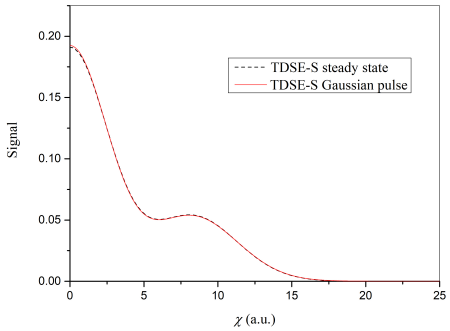

(b)

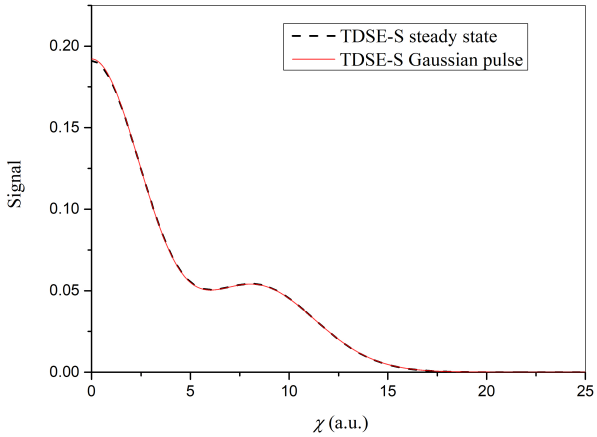

(c)

Fig. 22. *Cumulative signal for $\varepsilon = -0.951$, $F = 808$ V/cm and $m = 0$ at the detector (coupled channels $n_1 = 0, 1, 2, 3$) for a Gaussian pulse (Eq. (4.2)) with (a) $\tau = 10$ ps (b) $\tau = 121$ ps (c) τ =484 ps, compared with the steady state results.*

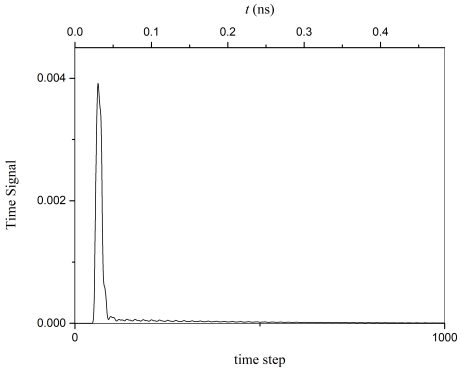

(a)

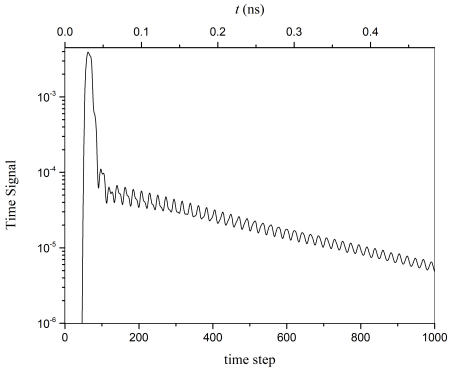

(b)

Fig. 23. *(a) The time signal at the detector for the case of a pulse, $\varepsilon = -0.9564$, $F = 808$ V/cm and $m = 0$ calculated using the channels $n_1 = 0, 1, 2, 3$. (b) the same signal with (a) in logarithmic scale.*

reduction in intensity over time reflects the resonance's lifetime. In order to examine if the solution for the pulse can rightly reproduce the steady state results, we need to test the cumulative signal (Fig. 24).

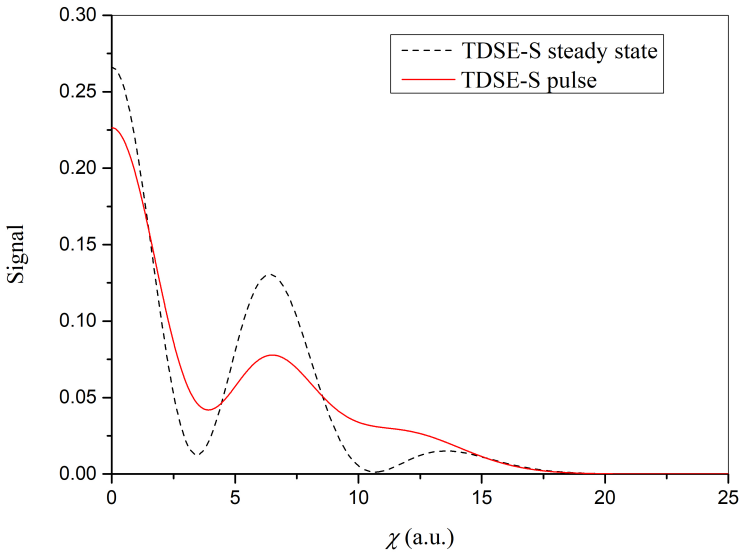

Fig. 24. *The cumulative signal for $\varepsilon = -0.9564$, $F = 808$ V/cm and $m = 0$ at the detector for the pulse of Eq.* (4.1) *(with $\tau \approx 10$ ps) and for $\varepsilon = -0.9564$, calculated using four channels ($n_1 = 0, 1, 2, 3$). The steady state results are also present for comparison.*

Short pulse duration easily explains the discrepancies with the steady state signal. However, as in the previous case ($\varepsilon = -0.951$), the results coincide if we increase the width of the pulse, as in Fig. 25.
We can testify that a pulse of ≈ 2.5 ns, leads the system to a state, that exhibits no further time evolution.

We arrive at the same conclusions with the Gaussian pulse of Eq. 4.2. Specifically, we can see that the steady state is reached even for $\tau = 1.21$ ns. So the duration of the pulse needs to be $\approx 1.5\times$ larger in comparison with the non-resonant energy, reflecting the larger time of life of the resonant.

The TDSE-S results are reasonable and within our physical intuition, a fact that proves the consistency of the method. This means that when we finally address the accuracy issues of the resonant channels, we can be confident for the validity of the results, coming from the pulse TDSE-S solution.

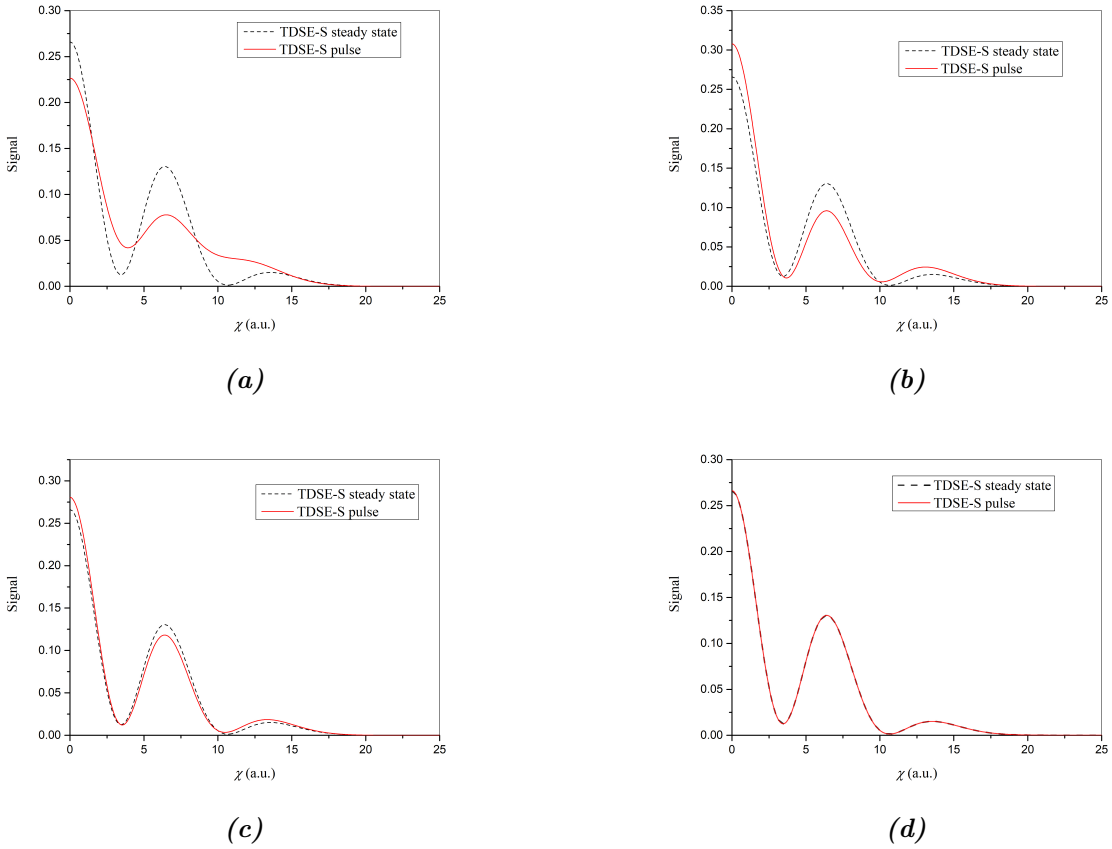

Fig. 25. *The cumulative signal ($\varepsilon = -0.9564$, $F = 808$ V/cm, $m = 0$ and the usual four coupled channels) for the pulse of Eq.* (4.1) *and for $\tau \approx$ (a) 10 ps (b) 0.5 ns (c) 1.25 ns (d) 2.5 ns*

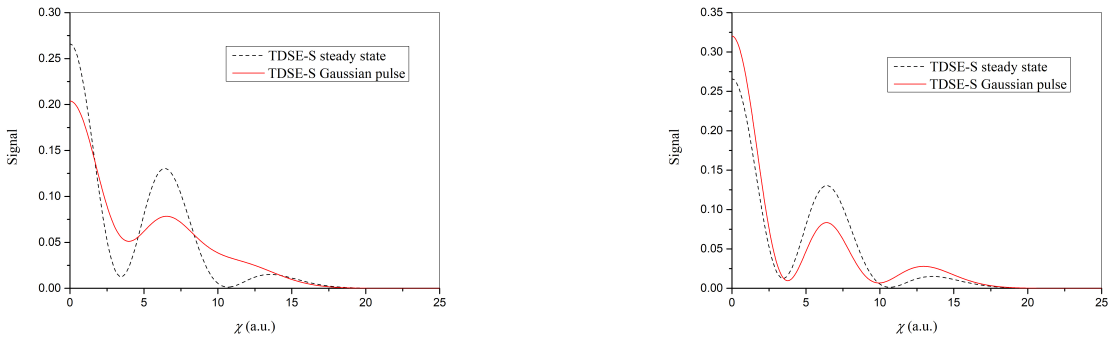

(a)

(b)

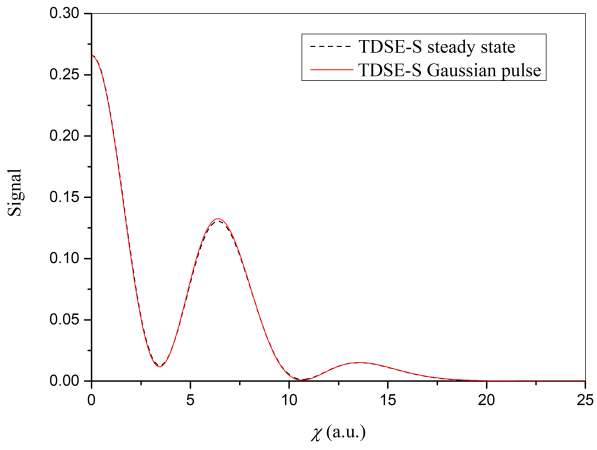

(c)

Fig. 26. *Cumulative signal for the resonant energy* $\varepsilon = -0.9564$, $F = 808$ V/cm *and* $m = 0$ *(calculated using* $n_1 = 0, 1, 2, 3$*) for the Gaussian pulse of Eq.* (4.2) *with (a)* $\tau = 10ps$ *(b)* $\tau = 0.24ns$ *(c)* $\tau = 1.21ns$.

5. Conclusions

We have successfully implemented a framework for the numerical solution of the time dependent Schrödinger equation (TDSE) for the case of near-threshold single-photon ionization of a hydrogen atom in a static electric field. Key novelties of the proposed solution are the utilization of the short time propagator and semi-parabolic coordinates for the spatial part. The latter allowed for a great reduction of the dimensionality of the final linear system to be solved. User-considerate numerical solutions have to use computational resources efficiently and this was implemented in this work by a carefully selected variable transformation (mapping) that optimally distributed the points of the spatial grid.

The computational framework consists of three interlaced autonomous programs, each with a modular design allowing for easy code optimization. In the first program, stationary near-threshold Stark state wavefunctions are computed, for fixed magnetic quantum number, field strength and energy of interest. This step allows the user to control the number of states to be included further in the computation and thus determine the dimensionality of the problem. The second program performs the time evolution thus providing the TDSE's solution, which is an outgoing, ionizing wavepacket. Additionally, it notably takes the necessary steps to avoid unphysical reflections at the edge of the spatial grid. Finally, the third program uses this computed wavepacket to calculate the probability current density of the photoionized electrons at the surface of a virtual position sensitive detector.

As a benchmark, the solution of the TDSE for a long, steady state pulse, has been compared to the known time independent solutions existing in literature and which are computed by the first program. Both qualitatively and quantitatively, the comparison is very promising for all energies with the exception of resonances. In these narrow energy intervals (resonances) quantitative agreement fails, however the basic expected behavior is still captured by our time-dependent calculation. The discrepancies regarding the resonances can be attributed to the existence of turning points in the wavenumber function, which are absent for the continuum states and are not considered by our mapping scheme. Finally, reliable results have been also obtained for the case of bell-shaped pulses, and it has been verified that for long enough pulse duration one recovers the steady state results.

Our observations so far call for specific further improvements. First, a new mapping function needs to be designed, that considers the wavenumber function particularities in the vicinity of resonances. Further, the application of a numerical method that solves the final linear system without the need of matrix inversion would allow the increase of spatial mesh points and hence increase the accuracy of the solution. It will also allow propagating the wavepacket at larger distances than in the present work. Moreover, the

implementation of THz pulses to the static electric field may be envisioned. Finally, it would be worth examining the extension of the present code to multiphoton transitions and multi-electron atoms.

Appendix: Steady State Solution of the Schrödinger Equation with a Source

As was mentioned earlier, when the system under study experiences a radiation field characterized by an envelope constant in time ($G(t) = 1,\ \forall\, t$), it reaches a steady state. The TDSE-S that describes the steady state is,

$$\left[-\frac{1}{2}\nabla^2 + U_{CS}(\mathbf{r}) - E\right]\psi^+_{out}(\mathbf{r}) = -\boldsymbol{\varepsilon}\cdot\mathbf{r}\psi_i(\mathbf{r}), \tag{A.1}$$

where the assumed form of the outgoing wavepacket is,

$$\psi^+_{out}(\mathbf{r}) = (2\pi\chi\upsilon)^{-1/2}\sum_{n'_1,m'} e^{im'\phi}X_{n'_1,|m'|}(\chi)y^+_{n'_1,m'}(\upsilon). \tag{A.2}$$

The $X_{n_1,|m|}$ wavefunctions obey Eq. (2.6) and follow the normalization of Eq. (2.10). By inserting (A.2) to (A.1), we get,

$$(y^+_{n_1,m}(\upsilon))'' + k^2 y^+_{n_1,m}(\upsilon) = 2g^m_{n_1}(\upsilon), \tag{A.3}$$

with

$$k_{n_1,|m|}(\upsilon) = [2(2Z_2^{n_1,|m|} - U_{Y,eff}(\upsilon))]^{1/2}, \tag{A.4}$$

and

$$g^m_{n_1}(\upsilon) = \int_0^\infty d\chi X_{n_1,|m|}(\chi)(\chi^2+\upsilon^2)\chi^{1/2}\upsilon^{1/2}\int_0^{2\pi} d\phi\frac{e^{-im\phi}}{(2\pi)^{1/2}}\boldsymbol{\varepsilon}\cdot\mathbf{r}\psi_i(\mathbf{r}). \tag{A.5}$$

Assuming now, without loss of generality, that the initial state ψ_i is a single state and of the form of Eq. (2.5), $g^m_{n_1}$ simplifies further as,

$$g^m_{n_1}(\upsilon) = Y_i(\upsilon)\int_0^\infty d\chi X_i(\chi)X_{n_1,|m|}(\chi)(\chi^2+\upsilon^2)\int_0^{2\pi} d\phi\ \boldsymbol{\varepsilon}\cdot\mathbf{r}\frac{e^{i(m_i-m)\phi}}{(2\pi)}, \tag{A.6}$$

with X_i and Y_i being the χ and υ component of the initial state, respectively. It can be shown that the solution of (A.3) writes,

$$y^+_{n_1,m} = -\frac{2d_{n_1,m}}{C_Y^2}[Y_2(\upsilon) + iY_1(\upsilon)]$$

$$-\frac{2}{C_Y^2}\left[\left(\int_\upsilon^{\upsilon_{i,lim}} g^m_{n_1}(\upsilon')Y_2(\upsilon')d\upsilon'\right)Y_1(\upsilon) - \left(\int_\upsilon^{\upsilon_{i,lim}} g^m_{n_1}(\upsilon')Y_1(\upsilon')d\upsilon'\right)Y_2(\upsilon)\right], \tag{A.7}$$

where Y_1 and Y_2 are the regular and irregular solutions of the Y-component of (2.6) that is

$$Y''_{n_1,|m|}(\upsilon) + k^2 Y_{n_1,|m|}(\upsilon) = 0, \tag{A.8}$$

which can be put in the form of the Milne equation [61],

$$\mathcal{M}''_{n_1,|m|}(\upsilon) + k^2(\upsilon)\mathcal{M}_{n_1,|m|}(\upsilon) - \frac{1}{\mathcal{M}^3_{n_1,|m|}(\upsilon)} = 0. \tag{A.9}$$

Then, Y_1 and Y_2 are given by,

$$Y_1(\upsilon) = C_Y Y_r(\upsilon) = C_Y \mathcal{M}_{n_1,|m|}(\upsilon)\sin(\theta_{n_1,|m|}(\upsilon) + \phi_{n_1,|m|})$$

$$Y_2(\upsilon) = C_Y Y_{ir}(\upsilon) = C_Y \mathcal{M}_{n_1,|m|}(\upsilon)\cos(\theta_{n_1,|m|}(\upsilon) + \phi_{n_1,|m|}), \tag{A.10}$$

with

$$\theta(\upsilon) = \int^{\upsilon} \frac{1}{\mathcal{M}^2(\upsilon')} d\upsilon', \tag{A.11}$$

while $\phi_{n_1,|m|}$ is a constant phase and C_Y is a (large distance) normalization constant,

$$C_Y = \sqrt{2/\pi}. \tag{A.12}$$

Finally,

$$d_{n_1,m} = \langle \psi_i | \, \boldsymbol{\varepsilon} \cdot \mathbf{r} \, | \psi^F_{n_1,m} \rangle = \int_0^{\infty} Y_{n_1,|m|}(\upsilon) g^m_{n_1}(\upsilon) d\upsilon, \tag{A.13}$$

is the dipole transition matrix element between the initial ψ_i and the final Stark state $\psi^F_{n_1,m}$. Thus, the problem is reduced to the knowledge of the solutions of the homogeneous equation (A.8) [19].

In (A.7) $\upsilon_{i,lim}$ is the coordinate value after which $Y_i(\upsilon)$, and consequently $g^m_{n_1}(\upsilon)$, have completely decayed,

$$g(\upsilon \geq \upsilon_{i,lim}) = 0. \tag{A.14}$$

Hence, Eq. (A.7) shows that for $\upsilon \geq \upsilon_{i,lim}$ the outgoing wave is given by,

$$y^+_{n_1,m}(\upsilon \geq \upsilon_{i,lim}) = -\frac{2d_{n_1,m}}{C_Y^2}[Y_2(\upsilon) + iY_1(\upsilon)] = -\frac{2d_{n_1,m}}{C_Y}\mathcal{M}_{n_1,|m|}(\upsilon)e^{i[\theta_{n_1,|m|}(\upsilon)+\phi_{n_1,|m|}]}. \tag{A.15}$$

In our computations we always place the detector at a distance $\upsilon_{det} \geq \upsilon_{i,lim}$ for any employed initial state. Hence, we use (A.15) for obtaining $y^+_{n_1,m}$ and the steady state electron current density, which is given by,

$$J_{\bar{\upsilon}}(\phi,\chi) = -\frac{1}{2\pi\chi\upsilon[\chi^2+\upsilon^2]^{1/2}}\mathrm{Im}\left[\sum_{n'_1,n_1,m',m} e^{i(m'-m)\phi} X_{n'_1,|m'|}(\chi)X_{n_1,|m|}(\chi)y^+_{n'_1,m'}(\upsilon)\frac{\partial}{\partial\upsilon}\left(y^+_{n_1,m}(\upsilon)\right)^*\right]\Bigg|_{\upsilon=\bar{\upsilon}}, \tag{A.16}$$

where by using (A.15), the term $y^+_{n'_1,m'}(\upsilon)\frac{\partial}{\partial\upsilon}\left(y^+_{n_1,m}(\upsilon)\right)^*$ becomes,

$$y^+_{n'_1,m'}(\upsilon)\frac{\partial}{\partial\upsilon}\left(y^+_{n_1,m}(\upsilon)\right)^* =$$

$$\frac{4}{{C_Y}^2} d_{n_1',m'} d^*_{n_1,m} \mathcal{M}_{n_1',|m'|} \left[\frac{\partial \mathcal{M}_{n_1,m}}{\partial \upsilon} - \frac{i}{\mathcal{M}_{n_1,m}} \right] e^{i[\theta_{n_1',|m'|}(\upsilon) - \theta_{n_1,|m|}(\upsilon) + \phi_{n_1',|m'|} - \phi_{n_1,|m|}]}. \quad \text{(A.17)}$$

If the condition $\upsilon_{det} \geq \upsilon_{i,lim}$ does not hold, then one may always use (A.7) which is valid over all space. In other studies, interested in large distances ($\upsilon \to \infty$), the relation (A.17) becomes simpler, given that Milne functions for large υ reduce to the WKB form,

$$\mathcal{M}_{n_1,|m|}(\upsilon) = \frac{1}{k^{1/2}_{n_1,|m|}(\upsilon)}, \quad \text{(A.18)}$$

where $k_{n_1,|m|}$ is given in (A.4). For $\upsilon >>$, the term $(4m^2 - 1)/(8\upsilon^2)$ in $U_{Y,eff}(\upsilon)$ can be neglected and hence,

$$k_{n_1,|m|} \approx \left[F\upsilon^4 + 2E\upsilon^2 + 4Z_2^{n_1,|m|} \right]^{1/2}. \quad \text{(A.19)}$$

When υ approaches infinity, even $4Z_2^{n_1,|m|}$ can be neglected, the Milne functions become independent of $|m|, n_1$ and the wavenumber becomes progressively large. Then, from Eq. (A.18), it is evident that as υ increases, Milne functions decrease, the derivative term in (A.17) can be approximated to zero and $\mathcal{M}_{n_1,|m|}/\mathcal{M}_{n_1',|m'|} \approx 1$.

References

[1]H. Bethe and E. Salpeter, *Quantum mechanics of one- and two-electron atoms* (Springer Berlin Heidelberg, 2013).

[2]T. Gallagher, *Rydberg atoms* (Cambridge University Press, 1994).

[3]V. D. Kondratovich and V. N. Ostrovsky, «Resonance and interference phenomena in the photoionisation of a hydrogen atom in a uniform electric field: I. resonances below and above the potential barrier», J. Phys. B: At. Mol. Phys. **17**, 1981–2010 (1984).

[4]V. D. Kondratovich and V. N. Ostrovsky, «Resonance and interference phenomena in the photoionisation of a hydrogen atom in a uniform electric field: II. overlapping resonances and interference», J. Phys. B: At. Mol. Phys. **17**, 2011–2038 (1984).

[5]V. D. Kondratovich and V. N. Ostrovsky, «Resonance and interference phenomena in the photionisation of a hydrogen atom in a uniform electric field: III. comparison with recent experimental and theoretical results», J. Phys. B: At. Mol. Opt. Phys. **23**, 21–43 (1990).

[6]R. J. Damburg and V. V. Kolosov, «A hydrogen atom in a uniform electric field», J. Phys. B. At. Mol. Phys. **14**, 829–834 (1981).

[7]E. Luc-Koenig and A. Bachelier, «Systematic theoretical study of the stark spectrum of atomic hydrogen. I. Density of continuum states», J. Phys. B: At. Mol. Phys. **13**, 1743 (1980).

[8]E. Luc-Koenig and A. Bachelier, «Systematic theoretical study of the stark spectrum of atomic hydrogen. II. Density of oscillator strengths. Comparison with experimental absorption spectra in solid-state and atomic physics», J. Phys. B: At. Mol. Phys. **13**, 1769 (1980).

[9]A. Alijah, J. T. Broad, and J. Hinze, «Stark effect and field ionisation of atomic hydrogen», J. Phys. B: At. Mol. Phys. **19**, 2617 (1986).

[10]A. Alijah, «Photoionization of atomic hydrogen in electric fields», J. Phys. B: At. Mol. Opt. Phys. **25**, 504–53 (1992).

[11]D. A. Harmin, «Theory of the Stark effect», Phys. Rev. A **26**, 2656–2681 (1982).

[12]D. A. Harmin, «Stark effect: Properties of the wave functions», Phys. Rev. A **24**, 2491–2512 (1981).

[13]Y. Hai-Feng, W. Lei, L. Xiao-Jun, and L. Hong-Ping, «Photoionization microscopy of hydrogen atom near a metal surface», Chin. Phys. B **20**, 063203 (2011).

[14]H.-F. Yang and Y.-G. Tan, «Time domain study on the tunneling dynamics in photoionization microscopy», J. Phys. B: Atom. Mol. Opt. Phys. **52**, 075008 (2019).

[15]H. Rottke and K. H. Welge, «Photoionization of the hydrogen atom near the ionization limit in strong electric fields», Phys. Rev. A **33**, 301–311 (1986).

[16]A. Kips, W. Vassen, and W. Hogervorst, «Application of closed-orbit theory to barium scaled-energy stark spectra», J. Phys. B: At. Mol. Opt. Phys. **33**, 109 (1999).

[17]V. D. Kondratovich and V. N. Ostrovsky, «Resonance and interference phenomena in the photoionization of a hydrogen atom in a uniform electric field: IV. differential cross sections», J. Phys. B: At. Mol. Opt. Phys. **23**, 3785–3809 (1990).

[18]P. A. Batishchev, O. I. Tolstikhin, and T. Morishita, «Atomic Siegert states in an electric field: transverse momentum distribution of the ionized electrons», Phys. Rev. A **82**, 023416 (2010).

[19]P. Kalaitzis, S. Danakas, F. Lépine, C. Bordas, and S. Cohen, «Photoionization microscopy: Hydrogenic theory in semiparabolic coordinates and comparison with experimental results», Phys. Rev. A **97**, 053412 (2018).

[20]S. Ohgoda, O. I. Tolstikhin, and T. Morishita, «Photoionization of hydrogen in a strong static electric field», Phys. Rev. A **95**, 043417 (2017).

[21]P. Kalaitzis, S. Danakas, K. Ferentinou, F. Lepine, C. Bordas, and S. Cohen, «Glory oscillations in photoionization microscopy: connection with electron dynamics and Stark spectral structures in the continuum», Phys. Rev. A **102**, 033101 (2020).

[22]C. Nicole, I. Sluimer, F. Rosca-Pruna, M. Warntjes, M. Vrakking, C. Bordas, F. Texier, and F. Robicheaux, «Slow Photoelectron Imaging», Phys. Rev. Lett. **85**, 4024–4027 (2000).

[23]F. Lépine, C. Bordas, C. Nicole, and M. J. Vrakking, «Atomic photoionization processes under magnification», Phys. Rev. A **70**, 033417 (2004).

[24]S. Cohen, M. M. Harb, A. Ollagnier, F. Robicheaux, M. J. Vrakking, T. Barillot, F. Lépine, and C. Bordas, «Photoionization microscopy of the lithium atom: wave-function imaging of quasibound and continuum Stark states», Phys. Rev. A **94**, 013414 (2016).

[25]P. Kalaitzis, S. Danakas, C. Bordas, and S. Cohen, «Near-saddle-point-energy photoionization microscopy images of Stark states of the magnesium atom», Phys. Rev. A **99**, 023428 (2019).

[26]S. Cohen, M. M. Harb, A. Ollagnier, F. Robicheaux, M. J. Vrakking, T. Barillot, F. Lépine, and C. Bordas, «Wave function microscopy of quasibound atomic states», Phys. Rev. Lett. **110**, 183001 (2013).

[27]A. S. Stodolna, A. Rouzée, F. Lépine, S. Cohen, F. Robicheaux, A. Gijsbertsen, J. H. Jungmann, C. Bordas, and M. J. Vrakking, «Hydrogen atoms under magnification: direct observation of the nodal structure of Stark states», Phys. Rev. Lett. **110** (2013).

[28]A. S. Stodolna, F. Lépine, T. Bergeman, F. Robicheaux, A. Gijsbertsen, J. H. Jungmann, C. Bordas, and M. J. Vrakking, «Visualizing the coupling between red and blue Stark states using photoionization microscopy», Phys. Rev. Lett. **113**, 103002 (2014).

[29]L. B. Zhao, D. H. Xiao, and I. I. Fabrikant, «Simulation of wave-function microscopy images of Stark resonances», Phys. Rev. A **91** (2015).

[30]P. Kalaitzis, S. Danakas, C. Bordas, and S. Cohen, «Manipulating slow photoelectron wave packets by rotation of the linear laser polarization», Phys. Rev. A **108**, 013106 (2023).

[31]G. M. Lankhuijzen and L. D. Noordham, «Frequency- and time-resolved study of the dynamics of rubidium rydberg wave packets in an electric field», Phys. Rev. A **52**, 2016–2028 (1995).

[32]C. Wesdorp, L. D. Noordam, and F. Robicheaux, «Dynamics of forced autoionization», Phys. Rev. A **60**, R3377–R3380 (1999).

[33]J. Murray-Krezan, J. Kelly, M. R. Kutteruf, and R. R. Jones, «Stark dynamics of two-electron atoms probed by scaled energy spectroscopy», Phys. Rev. A **75**, 013401 (2007).

[34]S. Cohen, P. Kalaitzis, S. Danakas, F. Lépine, and C. Bordas, «Photodetachment and photoionization rainbows and glories», J. Phys. B: Atom. Mol. Opt. Phys. **50**, 065002 (2017).

[35]K. Ferentinou, S. Danakas, C. Bordas, and S. Cohen, «Glory interference spectroscopy in Sr atom», J. Phys. B: Atom. Mol. Opt. Phys. **57**, 115002 (2024).

[36]P. Kalaitzis, S. Danakas, K. Ferentinou, S. Cohen, and C. Bordas, «Photoionization microscopy in the time domain: Classical atomic chronoscopy», Phys. Rev. A **110**, 013112 (2024).

[37]F. Robicheaux and J. Shaw, «Calculated electron dynamics in an electric field», Phys. Rev. A **56**, 278–289 (1997).

[38]F. Robicheaux and J. Shaw, «Erratum: Calculated electron dynamics in an electric field», Phys. Rev. A **94**, 029904 (2016).

[39]T. Topçu and F. Robicheaux, «Chaotic ionization of a highly excited hydrogen atom in parallel electric and magnetic fields», J. Phys. B: At. Mol. Opt. Phys. **40**, 1925–1949 (2007).

[40]B. C. Yang and F. Robicheaux, «Temporal interferences driven by a single-cycle terahertz pulse in the photodetachment dynamics of negative ions», Phys. Rev. A **92**, 063410 (2015).

[41]B. C. Yang and F. Robicheaux, «Closed-orbit theory for photodetachment in a time-dependent electric field», Phys. Rev. A **93**, 053413 (2016).

[42]B. C. Yang and M. L. Du, «Field-induced time modulation and bunching effects in photodetachment microscopy», Phys. Rev. A **108**, 023119 (2023).

[43]A. Ollagnier, «Microscopie de photoïonisation : une étude classique, semi-classique et quantique.», PhD thesis (Université Claude Bernard 1, 2007).

[44]M. Harb, «Microscopie de fonction d'onde électronique», PhD thesis (Université Claude Bernard 1, 2010).

[45]L. Landau and E. Lifshitz, *Quantum mechanics non-relativistic theory*, 3rd ed. (Pergamon Press, 1977).

[46]R. Szmytkowski and M. Gruchowski, «Ingoing and outgoing waves in the non-relativistic theory of photoionization», J. Quant. Spectrosc. Radiat. Transfer **94**, 127–136 (2005).

[47]C. A. Moyer, «Numerov extension of transparent boundary conditions for the Schrödinger equation in one dimension», Am. J. Phys. **72**, 351–358 (2004).

[48]M. Fox, *Quantum optics, an introduction* (Oxford University Press, 2006).

[49]F. L. Dubeibe, «Solving the time-dependent Schrödinger equation with absorbing boundary conditions and source terms in mathematica 6.0», Int. J. Mod. Phys. C **21**, 1391–1406 (2010).

[50]J. C. Light, I. P. Hamilton, and J. V. Lill, «Generalized discrete variable approximation in quantum mechanics», J. Chem. Phys. **82**, 1400–1409 (1985).

[51]V. Kokoouline, O. Dulieu, R. Kosloff, and F. Masnou-Seeuws, «Mapped Fourier methods for long-range molecules: application to perturbations in the Rb2(0u+) photoassociation spectrum», J. Chem. Phys., 9865–9876 (1999).

[52]D. T. Colbert and W. H. Miller, «A novel discrete variable representation for quantum mechanical reactive scattering via the S-matrix kohn method», J. Chem. Phys. **96**, 1982–1991 (1992).

[53]S. Danakas and S. Cohen, «Fisher information-based optimization of mapped fourier grid methods», Atoms **12**, 50 (2024), and references therein.

[54]M. Nest and H. D. Meyer, «Improving the mapping mechanism of the mapped fourier method», Chem. Phys. Lett. **352**, 486–490 (2002).

[55]V. V. Meshkov, A. V. Stolyarov, and R. J. L. Roy, «Adaptive analytical mapping procedure for efficiently solving the radial Schrödinger equation», Phys. Rev. A **78**, 052510 (2008).

[56]V. V. Meshkov, A. V. Stolyarov, and R. J. Le Roy, «Rapid, accurate calculation of the s-wave scattering length», J. Chem. Phys. **135**, 154108 (2011).

[57]D. Lemoine, «Optimized grid representations in curvilinear coordinates: the mapped sine Fourier method», Chem. Phys. Lett. **320**, 492–498 (2000).

[58]T. Fevens and H. Jiang, «Absorbing boundary conditions for the Schrödinger equation», SIAM Journal on Scientific Computing **21**, 255–282 (1999).

[59]X. Antoine, A. Arnold, C. Besse, M. Ehrhardt, and A. Schädle, «A review of transparent and artificial boundary conditions techniques for linear and nonlinear Schrödinger equations», Communications in Computational Physics **4**, 729–796 (2008).

[60]L. B. Zhao, I. I. Fabrikant, M. L. Du, and C. Bordas, «Test of the Stark-effect theory using photoionization microscopy», Phys. Rev. A **86**, 053413 (2012).

[61]W. E. Milne, «The numerical determination of characteristic numbers», Phys. Rev. **35**, 863–867 (1930).